Deposition and Characterisation of Perovskite Thin Films

Connor Gregory
@00572617

May 2021

1 Declaration

Type of Award: Master of Science

School: Science, Engineering and Environment

I declare that while registered as a candidate for the research degree, I have not been a registered candidate or enrolled student for another award of the university or other academic or professional institution.
I declare that no materials contained in this thesis has been used in any other submission for an academic award and is solely my own work. No proof-reading service was used in the compilation of this thesis.

Connor Gregory
May 2021

Contents

2 Acknowledgements

3 List of Acronyms

PV - Photovoltaic
PSC - Perovskite Solar Cell
PCE - Power Conversion Efficiency
LED - Light Emitting Diode
PL - Photoluminescence
MAPI - Methylammonium Lead Iodide
MA - Methylammonium (CH_3NH_3)
JTD - Jahn-Teller Distortion
UV-Vis - Ultraviolet-visible
HOIP - Hybrid Organic Inorganic Perovskite
FA - Formamindinium
LHPK - Lead Halide Perovskite
HTL - Hole Transport Layer
TCO - Transparent Conducting Oxide
MG - Micro Gel
J_{sc} - Short circuit current
V_{oc} - Open circuit voltage
FF - Fill factor
P_{in} - Power input
THz - Terahertz
EM - Electromagnetic
UOS - Ultrafast Optical Spectroscopy
CVD - Chemical Vapour Deposition
APCVD - Atmospheric Pressure Chemical Vapour Deposition
LPCVD - Low Pressure ”
UHVCVD - Ultra High Vacuum ”
PECVD - Plasma Enhanced ”
AACVD - Aerosol Assisted
CQD - Colloidal Quantum Dot
QD - Quantum Dot
r_B - Bohr radius
LARP - Ligand Assisted Re-Precipitation
XPS - Xray Photoelectron Spectroscopy
PLQY - Photoluminesence Quantum Yield
UOS - Ultrafast Optical Spectroscopy
VBM - Valence Band Maximum
CBM - Conduction Band Minimum

MEG - Multiple Electron Generation
TRPL - Time Resolved Photoluminescence
UTA - Ultrafast Transient Absorption
PIA - Photo-Induced Absorption
HTL - Hole Transport Layer
ETL - Electron Transport Layer
PD - Photo-Dember
IPA - Isopropyl Alcohol
FTO - Fluorine doped Tin Oxide
DMF - N,N Dimethylformamide
DMSO - Dimethylsulfoxide
CE - Corning Eagle
FWHM - Full Width Half Max
XRF - X-ray Fluorescence
XRD - X-ray Diffraction
SEM - Scanning Electron Microscopy
RSF - Relative Sensitivity Factor
F_Cl - Fresh Chlorine series
A_Cl - Aged Chlorine series
A_Br - Aged Bromine series

4   Abstract

The work presented in this thesis investigates the synthesis, deposition and characterisation of halide doped perovskite thin films. Films of methylammonium lead iodide $CH_3NH_3PbI_3$ were doped with Cl and Br ions to investigate the intrinsic differences of these perovskites. As a result of doping, photoluminescence (PL) spectra confirmed optoelectronic influence evidenced by changes in bang gap energy. Bromine treated perovskites exhibited greater stability throughout this study while Cl treated samples exhibited improved morphology. A detailed analysis comprising of scanning electron microscopy and bulk/surface elemental compositional techniques confirmed morphological improvement due to the presence of Cl ions despite being undetected using surface sensitive techniques.

5   Chapter 1

5.1   Introduction

Perovkite has quickly developed a reputation as an emerging photovoltaic (PV) technology, stemming from the dye-sensitized solar cells designed by Grätzel in 1991 [1]. Since then the scientific community has seen Perovskite solar cells (PSC) demonstrate power conversion efficiencies (PCE) of 3.81% [2] in 2009, rising to 25.2% [3] certified PCE in as little as 10 years. This unprecedented and rapid advancement has attributed to its reputation and has become its own category of light harvesting technology: pervoskite solar cells.
Perovskite possess some very impressive optoelectronic properties such as [4] : long charge carrier lifetimes, exceptionally large diffusion lengths, high electron and hole mobility and an energy gap of approximately 1.5 eV. These factors are beneficial because the greater the charge carrier lifetime and the greater the mobility, means more photocurrent can be harvested.

It is proving to be a great challenge in understanding the relationship between structure, composition and optoelectronic properties because, the fundamental physics behind these exciting photoelectric properties are obfuscated by photophysical processes and quantum coupling effects. [4] [5]

Research into perovskite seems dominated by solar cell application but, many other technologies can benefit from this material: tandem cell devices, LED's [6], Lasers [7], photodetectors and terahertz devices [8].

This study focuses on the synthesis, deposition and characterisation of lead halide perovskite thin films, using Aerosol Assisted Chemical Vapour Deposition (AACVD) and explores the stability and opto-electronic properties of single and mixed halide perovskite thin films.

Chapter 1, will provide an introduction to the structure and composition of what perovskite is, before discussing the archetypal forms of perovskite and the issues associated with this class of materials.

Chapter 2 will provide a theoretical description of thin film formation before elaborating on the various methods of synthesis and deposition commonly used within the scientific community and issues/results associated with these methods. Subsections of this chapter explore the excitation and recombination dynamics of charge carriers, applications of perovskite technology and provide a strong theoretical understanding of the characterisation methods used to analyse samples within this study.

Chapter 3 will provide the bulk of experimental work carried out in this project from substrate choice and preparation to the synthesis and deposition of multiple sample series'. While chapter 4 contains the results and discussion corresponding to each analytical technique used in this thesis.

A prominent issue in this study (and many others) is the detection of chlorine within treated samples of perovskite, despite clear optical and morphological influence due to the introduction of Cl. Elemental identifcation techniques such as X-ray Fluorescence Spectroscopy (XRF), Energy Dispersive X-ray Spectroscopy (EDX) and X-ray Photoelectron Spectroscopy (XPS) all failed in detecting a Cl signal, though potential explanations as to why have been offered within the relevant chapters.

5.2 Perovskite

The name perovskite describes the structure of a mineral named after Russian mineralogist Count Lev Von Perovski, following the discovery of naturally occurring perovskite, calcium titanate $CaTiO_3$ by Gustav Rose in 1839 [9]. Compounds with a Perovskite structure typically have the formula (ABX_3), where A and B represent the two larger cations and X corresponds to the negatively charged anion. In this study, lead halide perovskites will be studied (X = I^-, Cl^-, Br^-).

Candidates for the cations and anion can be suggested by employing the use of the Goldschmidt tolerance factor (t) [10]

$$t = \frac{R_X + R_A}{-2(R_X + R_B)} \tag{1}$$

Where R_X, R_A and R_B are the accepted values for the ionic radii of the A, B and X ions.

The tolerance factor provides a rough estimate of the stability and the distortion from the cubic phase. It is worth noting that assumptions are made regarding the precise ionic radii of the cations and anions, thereby reducing the reliability of this method for predicting novel perovskite structures. Despite this, it is generally well accepted that the values for the tolerance factor for halide perovskites are between $0.85 < t < 1.11$ [11].

As mentioned above, distortions away from the ideal cubic phase are sensitive to the ionic radii, it can be observed that smaller X anions can lead to a more stable cubic phase [12].The table below summarises the geometry corresponding to tolerance factor.
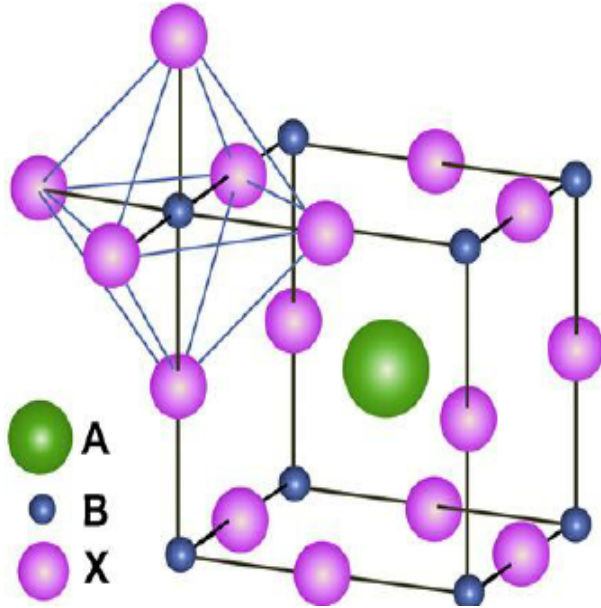
Figure 1 - Ideal cubic phase structure of ABX_3 perovskite [13].

Table 1: Goldschmidt tolerance factor and the corresponding perovskite structure variations. R_X, R_A and R_B correspond to the effective ionic radii of the anion, organic cation and inorganic cation, respectively. [14]

Tolerance factor	Structure
> 1	Hexagonal structure
0.9 - 1.0	(ideal) cubic perovskites
0.71 - 0.9	orthorhombic + variants
< 0.71	disordered arrangement of cations

An additional consideration to the formability of stable perovskite structures is the octahedral factor[15]:

$$\mu = \frac{R_B}{R_X} \tag{2}$$

Where R_B and R_X are the ionic radii of the B cation and X anion, respectively. An optimum ratio exists between $0.442 < \mu < 0.895$ [15].

5.2.1 A Cation

It is well established that structure directly influences the electronic properties of a material and even slight changes in lattice parameters can lead to significant changes in properties. The body-centered A cation (the larger of the two, consistent with ABX_3 structure) has large influence on the optical properties as varying sizes of this cation can expand or contract the entire lattice, changes in bond lengths between the B cation and X anion (B - X) have been attributed to changes in band gap energy.[16]

The polarisation of the A cation in Methylammonium lead iodide (MAPI) (MA = $CH_3NH_3^+$) is reported to be 2.29 D (where D is the dipole moment) [17] and a low polarity associated with the organic cation has been reported to enhance carrier lifetimes [5]. This has a polarizing effect on it's non-polar octahedral neighbours where by, interactions between charge carriers and other lattice ions in a polar environment result in strong electron-phonon coupling which is known to influence charge carrier separation, improved carrier lifetimes[18] [5] and high open circuit voltages[19].
A larger cation has exhibited a reduction in band gap for organic-inorganic perovskites (see table 2).

Table 2: Table illustrating how variation in A cation ionic radius affects the energy gap. Energy gap determined via photoluminescence (PL) measurements.

Perovskite	Ionic radius (pm)	Energy gap (eV)
$FAPbI_3$	253[20]	1.531[21]
$MAPbI_3$	217[20]	1.604[21]

More evidence [22] has shown that modifying the A cation does not directly influence the valence band edge as it is only sensitive to halide substitution. So A-site modification may have a large influence on the conduction band.

5.2.2 B Cation

The effective radius of the B cation has been reported in detail to increase the tolerance factor,[23] since the inorganic component of the perovskite is typically smaller than the A-site cation there is less disturbance to the bond lengths often providing enhanced sta-

bility. For the ideal cubic perovskite to exist, the tolerance factor mentioned earlier must be $0.9 \leq t \leq 1.0$ and thus extending this range will influence stability. Stability is an important factor as photo and moisture induced degradation are well known issues surrounding lead halide perovskites [24]. The choice of B-site cation has shown to improve stability, the further down the periodic table we go[17]. A summary of the influence of A-site and B-site cations on the energy gap is shown below:
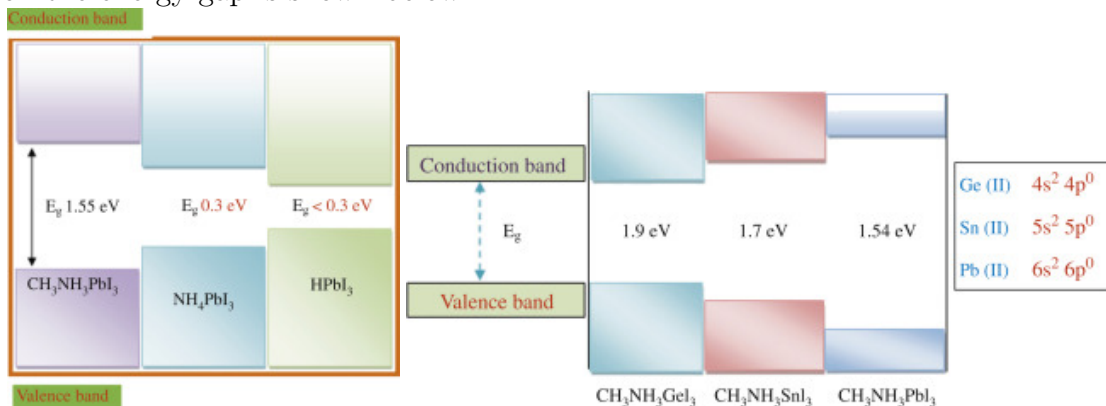
Figure 2. Illustrating influence of A-site cation (left) and B-site cation (right) substitution on the energy gap. [17]

5.2.3   X Anion

Changing the stochiometry of the X anion in perovskite can finely tune the band gap, evidence in literature has seen that doping with chlorine, bromine and iodine yields a reduction in the valence band energies[25]. Finely tuning the valence band can improve charge carrier transport properties and electron/hole mobility as well as improving stability due to changes in ionic size of halides.
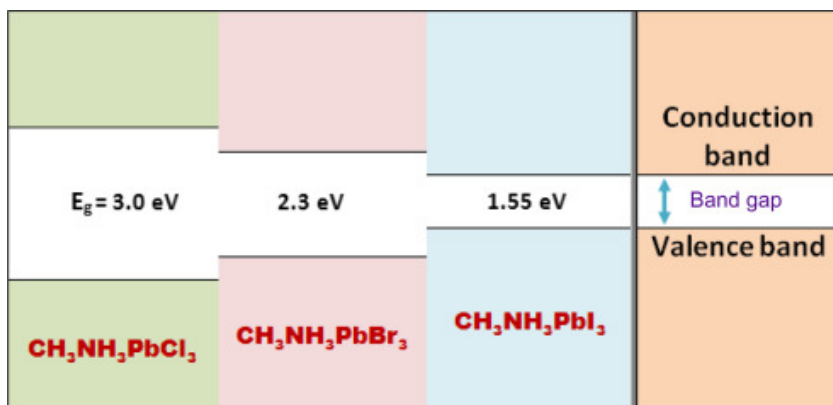
Figure 3. Illustrating the influence of X-site anion substitution on the band gap energy. [17]

5.2.4 Jahn-Teller Distortion

A Jahn-Teller Distortion (JTD) is a change in crystal geometry in order to improve stability. JTDs occur when ligands in a molecular system undergo contractions or elongations in order to lift electron degeneracy. In organo-metallic perovskites, the PbX framework can distort due to JTD of ligands with a z-component, as shown on the next page:
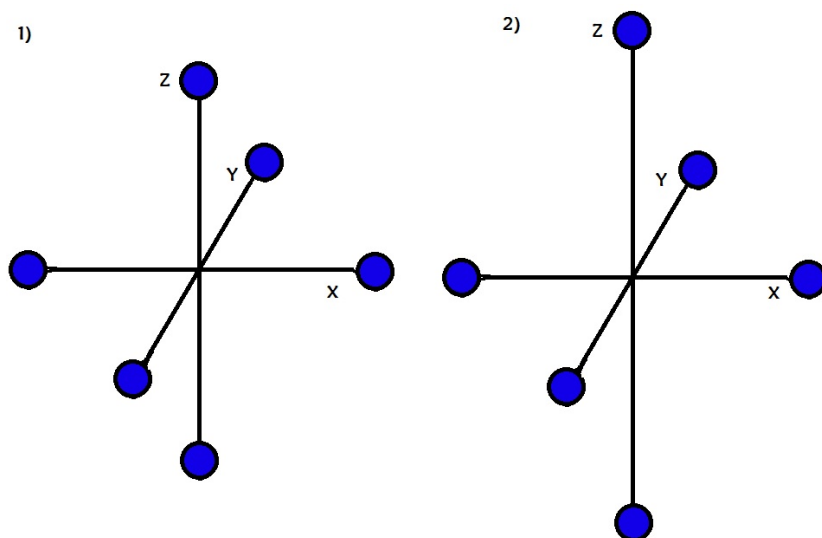
Figure 4. Basic illustration of a Jahn-Teller Distortion (JTD).
Image 1 (left) illustrates un-changed structure while image 2
(Right) shows an elongation in z-ligands due to JTD.

The distortion of the octahedral geomerty results in a more en-
ergetically favourable state, leading to a more stable system. In
perovskite structures, these distortions often result in elongations in
ligands with a z-component; as much as 25% from favourable ge-
ometry [26]. An elongation results in weaker interactions with the
inorganic cation and results in a more stable molecule.

5.3 Methylammonium Lead Iodide (MAPI)

There are many catalogued hybrid organic-inorganic perovskites (HOIPs) but among the most studied are methylammonium lead iodide ($CH_3NH_3PbI_3$) where CH_3NH_3 (methylammonium) represents the organic A cation, Lead corresponds to the inorganic B cation and X_3 the halide anion. Other examples include $CH_3NH_3PbI_2Cl$, $CH_3NH_3PbI_{3-x}Cl_x$, $CH_3NH_3PbI_{3-x}Br_x$, and $CH_3NH_3PbBr_3$.

Previous theoretical studies on the affect of halides on stability [22] show that halide substitution changes the Pb - X bond lengths, affecting structure. Below are the calculated and experimental lattice parameters for different halide perovskites.

Table 3: Table illustrating the theoretical lattice parameters and experimental parameters. Results show good agreement between theory and experiment. At room temperature (T=300K) Br and Cl perovskites adopt the cubic structure, while I perovskite adopts a tetragonal structure.

Perovskite	calculated bond lengths [22] (Å)	Experimental bond lengths (Å)
$MAPbI_3$	a = 6.33, b = 6.29, c = 6.39	a = b = c 6.39[27]
$MAPbBr_3$	a = 5.99, b = 5.96, c = 6.10	a = b= c 5.91[28]
$MAPbCl_3$	a = 5.71, b = 5.69, c = 5.85	a = b = c 5.68[28]

Research into alternative cation and multi-cation perovskite systems is also an active area of research. Mixed binary cation pervoskites using Formamindinium (FA) and Methylammonium (MA) $MA_xFA_{1-x}PbX_3$ have shown to affect morphology, optical and electronic properties resulting in a red shifted absorption edge and a higher short circuit current (J_{sc}) [29]. It has also been reported in ref [29] that FA has a passivating effect thus, increasing carrier lifetimes.

These molecular systems possess very interesting optoelectronic properties that are well suited to the enhancement of photovoltaic technology such as: long charge carrier lifetimes [30], large diffusion lengths [31], high charge carrier mobility, band gap tunability [4] and low exciton binding energies. Unfortunately though, the perovskites mentioned have been reported to be highly sensitive to light, moisture, heat and oxygen degradation [32] [24] so care must be taken in the synthesis and handling of the perovskite.

The decay chain of MAPI has been rigorously investigated, according to a review of the thermal stability of methylammonium lead halide pervoskites[33] the degradation pathway of MAPI by thermal channels is as follows:

$$CH_3NH_3PbI_3 \longrightarrow NH_3 + CH_3 + PbI_2 \qquad (3)$$
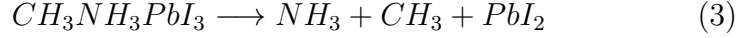
Other sources [34] suggest there are two main decomposition pathways for lead halide perovskites:

$$CH_3NH_3PbX_3 \longrightarrow PbX_{2(s)} + HX_{(g)} + CH_3NH_{2(g)} \qquad (4)$$

and

$$CH_3NH_3PbX_3 \longrightarrow PbX_{2(s)} + CH_3X_{(g)} + NH_{3(g)} \qquad (5)$$
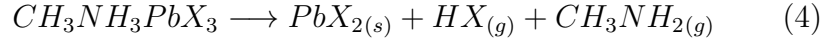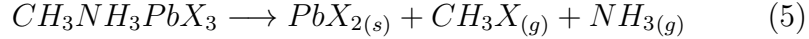
Where X corresponds to halide (I, Cl, Br).

5.4 $\quad CH_3NH_3PbI_{3-x}Cl_x$

The effect of Chloride treatment in Lead Halide Perovskites (LHPK) has also been widely studied and known to influence morphology [11] and improve charge transfer mechanisms [35]. However, studies have shown that Cl incorporation is only allowed at a few atomic percent [35]. Previous X-ray Photoelectron Spectroscopy (XPS) studies have consistently found thin films of $MAPbI_{3-x}Cl_x$ to show no presence of Cl, even at high Cl concentrations, or only observe a very weak signal. [35], [36]. The studies mentioned that the lack of Cl 2p signal is due to the limit of detection of the instrument, while ref [35] provided evidence that Cl is preferentially located towards the TiO_2 - PK interface. However, other sources [37] have suggested that organic Cl compounds such as MACl evaporate during the deposition process reducing the amount present in the sample.

probing depth is the main limiting factor of XPS due to the mean free path of the liberated electron and to circumvent this, the sample surface can be ablated by argon atoms revealing greater sample depths, which in itself alters the surface chemistry and morphology of the sample. But even after ablation the presence of Cl in mixed halide perovskites still evades detection for many [35].

Despite often undetectable presence, the role of Cl in perovskite has been thoroughly investigated[8] and the influence of chlorine on the electronic properties of MAPI are summarised in the table below:

Table 4. Summarising the effects of Chlorine doping on charge dynamics.

Perovskite	Charge Mobility ($cm^2V^{-1}S^{-1}$)	Diffusion length e-h (nm)	Exciton binding energies (meV)
$MAPbI_{3-x}Cl_x$	8	130 - 100	2 - 62
$MAPbI_3$	33	1069 - 1213	98

Table 4 above shows significant enhancement of charge mobility and diffusion length and thus charge carrier lifetime. A concentration of less than 4% (atomic) can have significant effects on the passivation of defects within LHPK [37] and Cl treatment of CdTe/Se quantum dots also exhibits enhanced charge dynamics due to the passivation effects of Cl on trap states. [5].

Cl incorporation, albeit in low concentration still has a dramatic effect on the PCE of perovskite solar cells [8], [37]. This is attributed to a number of factors including enhanced initial charge separation [38] and suppression of unwanted cooling pathways, resulting in a higher PCE. While higher and higher PCEs are being achieved, scalability and sensitivity to environment still remain a major limiting factor in the deployment of enhanced PV technology. However, mixed halide treatment such as Bromine doped MAPI ($CH_3NH_3PbI_{3-x}Br_x$) is known to improve stability and increase grain size [39] [40]. This can be further improved by the addition of Micro Gels (MGs) and capping agents [41]. Therefore, continued research is necessary to understand how to fix and improve these issues in order to unlock the full potential of perovskite enhanced PV technology.

6   Chapter 2

6.1   Synthesis and Deposition

So far there are two distinct approaches to synthesising perovskite and they are solution-based methods and vapour-based methods. Typically vapour phase methods have been reported to produce high

quality, pin-hole free, reproducible films but are disadvantaged by the cost to do such things. Factors such as high temperature and high vacuum add to the capital of vapour-based methods, though reliability to produce pristine thin-films have greatly assisted in the development of our understanding of perovskite.

Large scale fabrication of perovskite solar cells is an area of active research [42] [43] with different challenges to face. A couple issues with large scale fabrication are cost of materials, environmental sensitivity of product and reproducible pristine films. Aside from physical challenges, large scale also introduces device performance challenges as an increased surface area introduces bulk defects and an increased number of grain boundaries that act as recombination centers. These losses in photocurrent reduce open circuit voltage (V_{oc}), short circuit current J_{sc} and thus the maximum obtainable power from the device, quantified by the Fill factor (FF). This of course is not very good for the efficiency of solar cells. One study [43] managed to fabricate a perovskite solar cell close to $2m^2$ area, but with an efficiency of 6%. A few suggested methods for improving large scale efficiency are by changing chemical composition, deposition technique, or modify interfaces.

Various deposition techniques have resulted in varying degrees of control of the resultant film, below we discuss various synthesis techniques and their advantages and limiting factors.

6.2 CVD

Chemical vapour deposition (CVD) is a low cost, facile method of reacting gaseous chemical precursors to form a solid product. CVD is an attractive option as processing lines already exist within industry, is scalable and allows for simple mixing of multiple precursors. A typical CVD set-up consists of a variable inert carrier gas flow, a reaction/deposition chamber and an exhaust to ventilate unreacted products. Many variants of CVD have been developed such as: Atmospheric Pressure CVD (APCVD), Low-Pressure (LPCVD), Ultra-High Vacuum (UHVCVD), Plasma Enhanced (PECVD), Aerosol Assisted (AACVD). The method employed within this study is AACVD.

6.3 AACVD

AACVD uses an ultrasonic humidifier to atomise a liquid precursor solution which is then transported to the reaction zone via carrier gas (in this case N_2), the temperature inside the reaction zone causes rapid evaporation/decomposition forming vapours which then react and decompose onto the substrate.
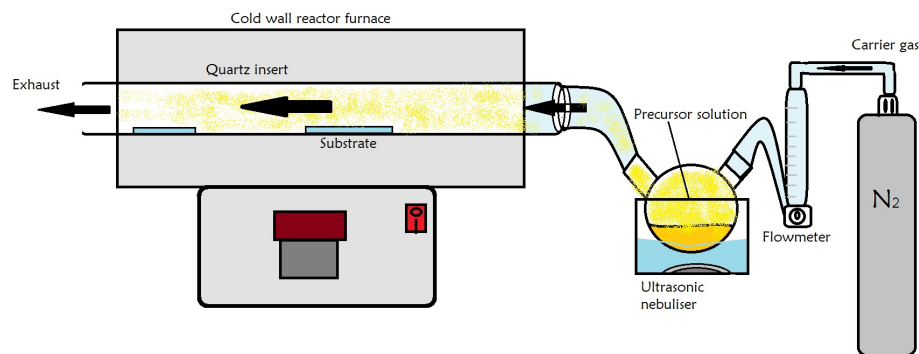
Figure 5. A very basic schematic of Aerosol Assisted Chemical Vapour Deposition (gas flow from right to left).

AACVD can undergo two kinds of reaction; the first, a heterogeneous reaction where by the vaporised precursor decomposes to form an intermediate species which then adsorbs onto a substrate and further reactions result in the film formation. On the other hand, a homogeneous reaction happens when the precursor mist decomposes early (gas-phase nucleation) and results in the deposition of a slightly porous film, this typically occurs at higher temperatures.
AACVD allows excellent control over surface density, film thickness, structural, morphological and optical properties due to the wide range of variable parameters like deposition time, temperature, carrier gas flow rate, substrate and pressure.

Early cases depositing MAPI via AACVD performed by Bhachu et al [44] resulted in powdery deposits but were compositionally uniform. Investigations into the effect of the critical parameters on the resultant film have been extensively studied, however different groups report different optimum deposition temperatures. for

example, Bhachu et al [44] reported the optimum deposition temperature to be 200°C and previous work by Yates et al [45] reported a set-point deposition temperature of 250°C, though thermocouple measurements for this study suggest the actual substrate temperature was closer to 230°C. This is attributed to the method used to heat the substrate, the latter using a hot wall rather than a cold wall furnace.

6.3.1 Film Growth

The substrate choice can be a range of materials including glass, plastic, or metal. The choice of substrate has a very strong influence on the resultant film morphology and adhesion. Any oil or surface contaminants can prevent material settling on the substrates surface and introduce unnecessary thermal stresses resulting in cracked films and pin-holes.

The interfacial morphology of the substrate can play a key role in the formation of thin films and the the substrate has been reported to influence bulk properties of perovskite, such as lattice parameters, grain orientation and grain size [46]. It has been found that substrates require passivation before perovskite film can start forming; depending on substrate this can be between 3 and 30 nm of deposited material before full substrate passivation [47]. Film formation can be broken down into several steps [48].

6.3.2 Surface Diffusion

Surface diffusion refers to the motion of the adsorbant atoms at the substrate surface moving from higher concentration to lower concentration and there are a few mechanisms for this depending on the amount of surface coverage. However, the most generic is hopping and or jumping in which the adsorbed species 'hops' to its nearest neighbour adsorbing site or jumps to its non-nearest neighbour site. This allows for clusters of the adsorber species to form and if the clusters are stable, leads to film formation.

6.3.3 Nucleation

Nucleation describes the local formation of a distinct thermodynamic phase and there are two distinct types of nucleation reactions, heterogeneous and homogeneous, as mentioned earlier. Heterogeneous nucleation is the most common form of reaction as compared to homogeneous and requires a nucleation site in order to undergo phase transformation. At these sites, the surfaces energy is lower and thus reduces the energy barrier allowing nucleation. This allows the formation of a spherical cap, analogous to a water drop (known as the capillarity model).

The preferable reaction in this situation is heterogeneous, as homogeneous reactions tend to result in gas phase nucleation which produces typically powdery deposits [44] using AACVD. However, efforts were concentrated on improving surface coverage and overall morphology by introducing more cleaning steps and modifying the choice of substrate, this can be seen in section 10.1.1.
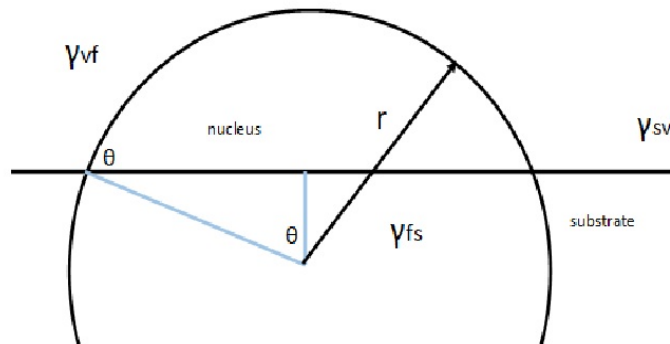
Figure 6. Illustration of the assumed spherical cap upon a substrate, where γ_{vf} is the surface energy between the vapour and film, γ_{fs} is the surface energy between the film and substrate.

The substrate or surface promotes nucleation due to wetting - the ability for a liquid to keep in contact with the substrate. For this, there are two factors that are in competition, the volumetric free energy (from the drop) and the surface energy of the substrate.

22

This can be expressed mathematically as follows:

$$\Delta G_{(r)} = V_f \Delta G_{(v)} + \gamma_{vf} A_{vf} + (\gamma_{fs} - \gamma_{vs}) A_{fs} \tag{6}$$

Where $\Delta G_{(r)}$ is the Gibbs free energy of the system, V_f is the volumetric free energy, γ_{vf} is the surface energy between vapour and film, A_{vf} is the interfacial area between vapour and film, γ_{fs} is the surface energy between the film and substrate and $\gamma_v s$ is surface energy between vapour and substrate. By substituting in the components of volumetric and surface energy, yields:

$$\Delta G_{(r)} = \frac{\pi r^3}{3} [2 - 3cos(\theta) + cos^3(\theta)] \Delta G_v + \gamma_v f \pi r^2 [1 - cos(\theta)] \tag{7}$$

Calculus derives the free energy for heterogeneous nucleation and is set equal to the energy required for homogeneous nucleation multiplied by a function of the contact angle θ called the wetting factor.

$$\Delta G_{het}(r) = \Delta G_{hom}(r) * f(\theta) \tag{8}$$

where

$$f(\theta) = \frac{2 - 3cos(\theta) + cos^3(\theta)}{4} \tag{9}$$

and

$$\gamma_{sv} = \gamma_{fs} + \gamma vf Cos(\theta) \tag{10}$$

From this, by differentiating equation 8 we yield an expression for the critical radius r^*

$$r^* = -\frac{2\gamma_{vf}}{\Delta G_v} \tag{11}$$

below the critical radius, the nucleus is more likely to disintegrate into gas phase, while above the r^* the nucleus is more likely to lead to further growth by reducing the free energy leading to a stable cluster forming.

6.3.4 Island Growth

The relative surface energies strongly influence nucleation leading to three main types of crystal growth: a) Frank van der Merwe (Layer by layer), b) Volmer-Weber (island growth) and c) Stranski-Krastanov (a combination of both).

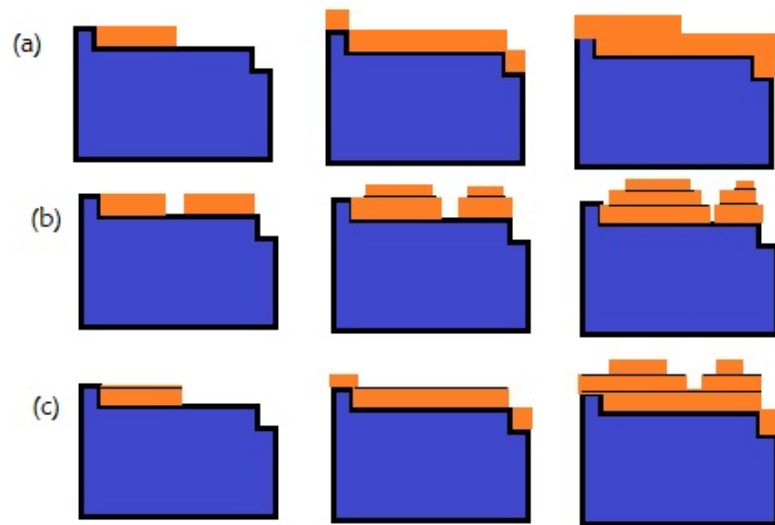Figure 7. Illustration of the three described growth processes a) Frank van der Merwe, b) Volmer-Weber and c) Stranski-Krastanov.

The table below summarises the growth mechanisms mentioned on the previous page.

Table 5. Growth mechanism as a function of contact angle.

Growth mechanism	Theta value	Result
Frank van der Merwe	$\theta = 0$	Particles bond more strongly with substrate than each other.
Volmer-Weber	$0 < \theta < 90$	Particles more tightly bound to each other than substrate.
Stranski-Krastanov		Subsequent growth of monolayer to form islands.

The growth mechanism for MAPI perovskite depends on the method used to synthesise the film. Epitaxial methods such as thermal evaporation have successfully synthesised layer-by-layer perovskites[49]. However, these techniques usually require high vacuum and high capital in order to produce such pristine films. This study has observed distinct island formation as a result of AACVD synthesis.

6.4 Colloidal Synthesis and Quantum Dots

Colloidal Quantum Dots (CQDs) are nanometre sized crystals of a semiconductor material, the terms nanocrystals and quantum dots are often used interchangeably. Colloidal synthesis is a solution based technique and the archetypal methods are: hot injection, non injection heating and decomposition of a single source precursor. Due to the nano scale nature of QDs, $(r_B < 4nm)$ quantum size effects start to manifest as a separation of valence band and conduction band energy states into discrete values for electrons and holes. The band gap can be tuned by controlling the size of the QD and the size can be controlled by isolating nucleation and growth processes such as reaction time, temperature and concentration[5]. Lead halide perovskite QDs have been synthesised via the Ligand Assisted Reprecipitation Technique (LARP) displaying full spectral tunability by controlling size and halide substitution [50]. LARP involves mixing $CH_3NH_3PbX_3$ precursors with DMF and the addition of a passivating organic ligand such as oleic acid and mixing it vigorously with a poor solvent such as toluene or hexane. The long chain ligands assist in the passivation of the QDs and have shown to dramatically improve PLQY in LHPK from 0.1% to approximately 70% [50] enhancing PL emission and stability.

However, even procedurally identical synthesis can result in varied size distributions, trap density and trap energy distributions within

the ensemble of QDs. Geometry, size and degree of passivaiton heavily influence electronic properties. So, further research into the ability to control the synthesis of QDs with a great deal of accuracy is vital to the development of these exotic materials.

6.5 Spin Coating

Spin coating seems to be the archetypal lab method for the synthesis of perovskite films, with at least 24 groups publishing papers with "spin coating" in the title between 2018 and 2020. Compared with other publications possessing "CVD" or "casting" in the title.
Typically, a small substrate approximately $2cm^2$ is placed into the centre of a stage (see figure 8) and is then spun at a few thousand rpm for a short time ($\leq$ 1min). As the substrate spins, the precursor solution is added drop-wise to the centre of the substrate and is uniformly spread across the surface due to the reaction of the centripetal force. The thickness of the resultant film does depend on the nature of the precursor (viscosity, concentration and surface tension) but the critical parameters of this process are the substrate dimensions and spin speed/duration.

Figure 8. Illustrating a spin-coater.

Spin coating is a reliable method that offers highly reproducible, uniform and generally high quality thin films. However, the main limiting factor of this method is the scalablity. As the substrates become larger, forces in the substrate become unbalanced and have a detrimental effect on the resultant film.

6.6 Photo-physical Mechanisms

In order to understand how perovskite can enhance PV technology, we must explore the dynamics of charge carriers and excitons with a particular focus on the recombination and associated timescales.

Excitons in MAPI exist in two types; Frenkel type and Wannier type. Frenkel type excitons have high binding energies, low Bohr radii and originate from the organic cation while Wannier type excitons possess large Bohr radii, low binding energies and originate from the inorganic sublattice. The population of excitons has been

known to change depending on the dimensionality of the system, due to quantum confinement effects, [51] with exciton energy increasing as dimensionality decreases. The exciton binding energy and exciton Bohr radius of MAPI is reported to be between 2 - 62 meV and $r_B = 22\mathring{A}$ [52]. This energy range is comparable to the thermal energy at room temperature $K_B T = 26 meV$ suggesting a fraction of excitons are able to dissociate into free carriers at room temperature. Following photoexcitation, the excitons can recombine in a number of ways, each with an associated timescale.

Table 6. A table of recombination processes and their associated timescales.

Recombination	Timescale	Comment
Radiative	ns to a few μs	
Trap assisted (1)	ps (similar for hot and cold trapping)	Influenced by morphology
Multiexciton (2)	10^1 - 10^2ps	Influence of halide ions
Auger (3)	10^1 ps	Significant at high carrier concentrations

The information in table 6 can be summarised as radiative and non-radiative recombination processes - the non radiative processes are a lot faster and share similar lifetimes which severely obscures identification of relaxation process in Ultrafast Optical Spectroscopy (UOS).

Relaxation processes are dominated by carrier-phonon coupling (Fröhlich interactions) and obey the rate equation:

$$\frac{dn_\tau}{d_\tau} = -k_1 n - k_2 n^2 - k_3 n^3 \tag{12}$$

Where k_1, k_2 and k_3 correspond to first, second and third order recombination processes as listed in the table above. By fitting carrier density to the rate equation, the dominant processes and associated rate constants can be determined.

6.7 Trap States

A trap state is an energy state the falls between the Valence Band Max (VBMax) and the Conduction Band Min (CBMin) and can form due to lattice defects, impurities or breaks in symmetry (interfaces). Trap states allow a non-radiative cooling pathway for ex-

cited charge carriers which competes with beneficial processes such as Photoluminescence Quantum Yield (PLQY) and Multiple Exciton Generation (MEG). The effects of trap states on recombination can be minimised by employing passivation techniques, such as the Ligand Assisted Reprecipitation (LARP) technique or shelling, which reduce the number of available traps thus, reducing unwanted cooling pathways. Passivation renders the chemical surface of the semiconducting material inert while maintaining its optoelectronic properties and can be used to improve stability. By reducing the number of traps, the number of available vacancies for oxidation will also decrease. It has been shown that the level of oxidation is negatively correlated with PLQY and even small amounts of oxygen contamination can introduce trap states that provide alternative, un-wanted relaxation processes such as Auger relaxation. [5].

Lead based perovskite nanocrystals have been treated with halides to give well passivated surfaces, resulting in a significant increase in quantum yield [5]. Halide treatment of MAPI has also shown to have a profound effect on the morphology of the film, resulting in smoother and more uniform films. Morphological improvements reduce the number of grain boundaries which also act as recombination centres (trap states).

Therefore, by controlling the degree of passivation during synthesis and handling, unwanted cooling pathways can be almost eliminated and lifetimes of carriers can be extended. This passivation effect is what is attributed to the enhanced lifetimes and diffusion lengths of charge carriers in chlorine treated MAPI.

6.8   Applications

So far, interest in applications of perovskite seem dominated by solar cell technology but many technologies can benefit from understanding this materials such as lasers, diodes, photodetectors and terahertz devices. The fundamental physics of semiconductors can be exploited in a number of ways.

6.9   Perovskite Solar Cells

There are two main architectures adapted for Perovskite solar cell (PSC) design - planar and mesoporous. See figure 9 below:
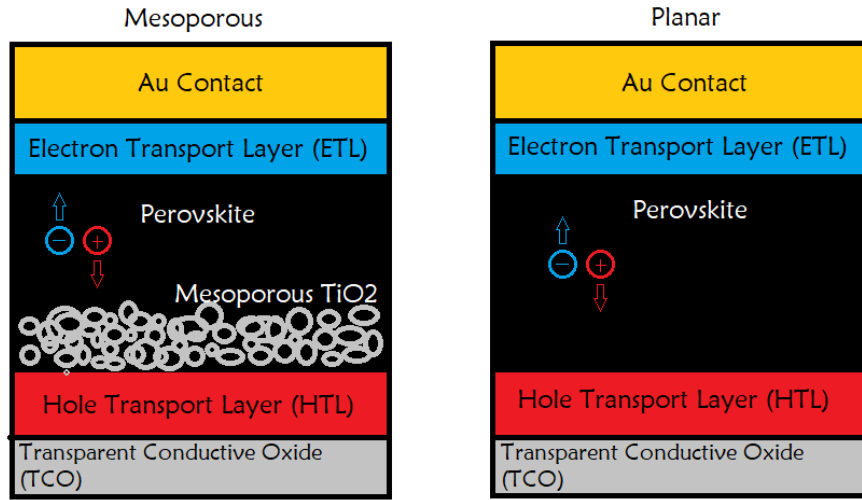
Figure 9. Showing difference between mesoporous (left) architecture and planar (right). Perovskite is deposited on a mesoporous scaffold of TiO_2 or Al_2O_3.

While both structures have produced high efficiency devices, the inherent advantages of either structure are still not well defined. Although, a comparative study of the utilisation of each architecture has shown that the planar structure exhibit longer radiative recombination lifetimes, as well as higher carrier mobility. This is attributed to the size of the grain boundaries as in the same report, the mesoporous structure seemed to restrict grain growth. [53] Restricted grain growth results in a lower mean crystal size and thus, an increase in grain boundaries, which are detrimental to performance. The power conversion efficiency (PCE) of a perovskite solar cell can be quantified using the equation below:

$$PCE = J_{SC} \cdot V_{OC} \cdot \frac{FF}{P_{in}} \tag{13}$$

Where J_{SC} is the short circuit current, V_{OC} is the open circuit voltage, FF is the fill factor and P_{in} is the power supplied to the cell.

A comparative study[54] was performed, investigating the compatibility of various perovskites with solar cell architecture. The study found that MAPI solar cells exhibited a higher V_{OC}, J_{SC} and fill factor adopting a meso-structured device. This was attributed to the meso-structure providing more efficient charge extraction due to the large interfacial area of perovskite infiltrated through the charge conducting scaffold. Planar structure (no scaffold) charge generation and extraction occurs in the perovskite layer upon photoexcitation.

Literature has provided evidence [38] that chlorine treated perovskite is more compatible with the planar architecture due to the long and balanced charge carrier mobilities in Cl treated perovskites.

6.10 Characterisation

6.10.1 UV-VIS Spectroscopy

UV-Vis spectrscopy is a fast and easy optical characterisation technique that measures the amount of light that is transmitted and reflected of a sample across a range of wavelengths. This was one of the main characterization techniques used extensively in this study. The transmission and reflection measurements were performed using an Aquila NKD 8000, operating between $\lambda = 350nm - 1000nm$ at an incident angle of $\theta = 30°$ p-polarised. Light across this range is incident on the sample and the percentage absorption can be quantified via the relation,

$$A = 1 - T - R \tag{14}$$

Where A is the absorptance and T and R are the measured transmission and reflection, respectively. Absorption occurs when the incident light is equal to or exceeds the band gap energy of the material and/or it's impurities. thus, from equation (14), band gap energies of the sample material can be estimated in the form of a Tauc relation (see results P42 for Tauc plots).

Figure 11. Image of the Aquila NKD-8000 used in this study. A) beam tube, B) Transmittance detector, C) Reflectance detector and D) Sample stage. UV-Vis has been routinely used for the characterisation of MAPI exhibiting an absorption edge occurring at approximately 770 nm.

6.10.2 Photoluminescence Spectroscopy

Photoluminescence (PL) spectroscopy is an analytical technique that allows the probe of discrete energy levels following excitation of a sample material. A light source of known wavelength (and hence energy) is being used to photo-excite the material; in the case reported here that was with the use of a 532 nm laser source. The incident photons are absorbed by the electrons promoting them to a higher energy state and then relaxing back to equilibrium resulting in the emission of a photon (radiative recombination) or without any photon emission through unwanted non-radiative transitions[55].

PL spectroscopy is considered a non-destructive analytical technique, however, sample degradation due to laser irradiation has been evident within this study (see chapter 12, P58). Aside from this, PL is a highly useful technique that allows semiconductor band gap

determination, impurity level and defect detection, probing of recombination mechanisms and surface structure excited states.

Radiative transitions in semiconductors involve defects within the local environment and thus the spectral peaks of impurities may be contained within the main peak which leads to broadening. Although PL can produce the optical signatures of the defects, no information can be revealed about their concentration or nature. Composite information generated by this method, as well as structural characterisation techniques is invaluable to assisting the understanding of the relationship between structure and function, ultimately accelerating the progress to 'designer' photovoltaics.

PL spectra were collected using a single grating HORIBA Jobin Yvon iHR320 spectrometer with nitrogen-cooled HORIBA Jobin Yvon Symphony CCD. An optical breadboard was setup as seen in the figure below:
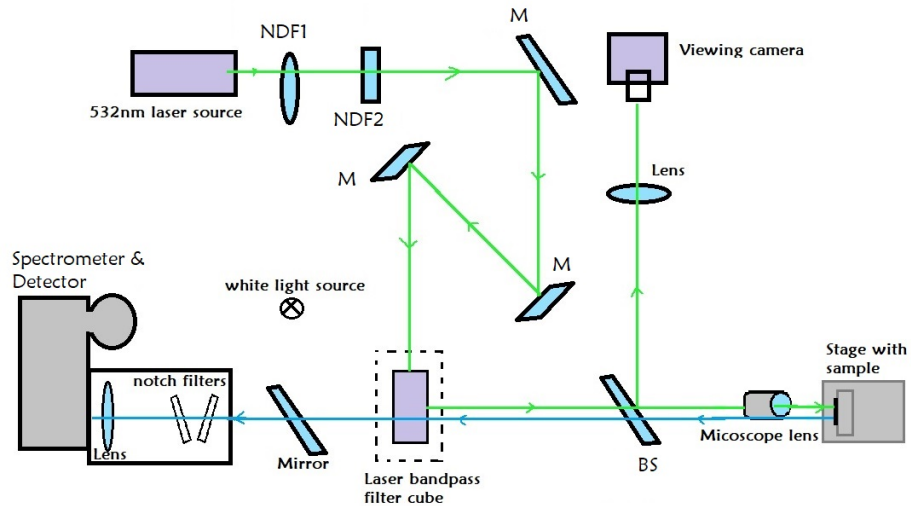
Figure 12. Optical breadboard PL system illustration. Where NDF1 - neutral density filter wheel for precise attenuation of laser beam. NDF2 - neutral density filter lens to further attenuate laser beam. BS - beam splitter. M - mirrors.

Firstly, the system was calibrated by placing a silicon reference sample at the focal point of the microscope lens and a quick spectrum was recorded. Once calibrated, samples were adhered to a vertical, micrometer controlled stage and the laser was focused onto the sample with aid of the viewing camera. Due to the photosensitive equip-

ment, alignment and focusing could be aided with the white light source, while working in the dark. Once focused, the 50:50 BS was removed from the photon path and the resolution and integration time was set. NDF1 and NDF2 could be adjusted to produce spectra with appropriate counts. Collection of data could be improved by selecting 1 of 2 diffraction gratings within the spectrometer, a 1500 lines/mm and a 300 lines/mm grating. The 1500 lines/mm grating was used for improved resolution when taking spectra. The 300 lines/mm grating was used to boost counts of clear signals compared to the higher resolution grating.

6.11 X-ray Photoelectron Spectroscopy (XPS)

X-ray Photoelectron Spectroscopy (XPS) was performed on a Thermo Fisher Scientific K-alpha spectrometer. Samples were analysed using a micro-focused monochromatic Al X-ray source (72 W) over an area of approximately 400 microns. Data was recorded at pass energies of 200 eV for survey scans and 40 eV for high resolution scan with 1 eV and 0.1 eV step sizes respectively. Scans were performed both before and after a 30 s (4 keV) argon etch to remove any surface contaminants. Charge neutralisation of the sample was achieved using a combination of both low energy electrons and argon ions.

XPS is a surface sensitive analytical tool, capable of determining the elemental composition, the chemical and electronic state of the element and their binding energies. XPS generates spectra by irradiating a sample with soft X-rays and measuring the kinetic energy of the electrons that are liberated from the sample. The detected energies produce a spectrum with characteristic peaks that correspond to the characteristic electron structure of the element.

XPS works on the principle of the photo-electric effect established by Hertz in 1887[56] noting that a material will charge under the illumination of UV light. This effect was then described and elaborated upon as the photo-electric effect by Einstein in 1905[57]. The mathematical description related the kinetic energy of the liberated electron to the frequency of the radiation as follows:

$$K_{max} = E_\gamma - \phi \tag{15}$$

Where E_γ is the energy of the photon which is proportional to the frequency 'ν' by Planck's constant 'h'.

$$K_{max} = h\nu - \phi \tag{16}$$

K_{max} is the maximum kinetic energy and ϕ is the work function intrinsic to the material. The work function is the minimum energy required to liberate an electron.

$$\phi = h\nu_0 \tag{17}$$

Where ν_0 is the minimum frequency required to release an electron. Since ϕ is a function unique to the element and suppose a constant photon energy is maintained, different elements with characteristic work functions will lead to characteristic kinetic energies of liberated electrons. This lead to the development of XPS by Kai Seigbahn in 1957.

6.11.1   X-ray Generation

X-rays can be generated a number of ways but lab based systems typically adopt the following [58]:
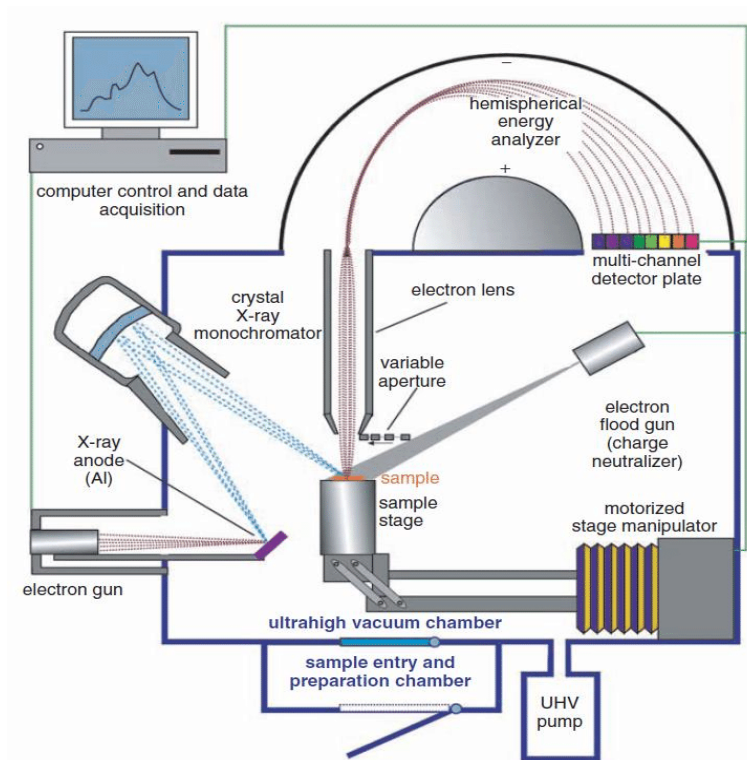
Figure 13. Annotated illustration of an XPS system.

Electrons are accelerated via thermionic emission towards a rotating anode (typically Al or Mg for XPS systems) which then collide with the target material. The incoming electron knocks out a core shell electron resulting in a hole which is then filled by an outer shell electron and the excess energy is radiated away as light.

The Bohr model of an atom states that a photon is produced when an electron transitions from an initial energy to a lower, final energy and the energy of the photon produced is equal to the difference between energy levels:

$$E_i - E_f = E_\gamma = h\nu \tag{18}$$

generally this can be written as:

$$E_\gamma = -E_1\left(\frac{1}{n_f^2 - n_i^2}\right) \tag{19}$$

where E_1 is the energy of the ground state (n=1) and n is the principal quantum number which describes the size of the orbital.

The generated X-rays are directed towards a monochromator and then directed towards the sample. The liberated electrons are focussed towards the detector and the kinetic energy is measured.

6.11.2 XPS Spectrum

In this case the radiation used for XPS was Al k(α) = 1486.6 eV corresponding to a transition from the 2p shell to the 1s shell (L-K transition in Seigbahn notation). The incoming photons liberate electrons residing in the top 10 nm of the material which are then directed to the detector and the resulting energy spectra exhibit resonant peaks characteristic of the electronic structure.

In observed spectra, electrons originating in orbitals greater than s-levels exhibit a doublet peak with slightly different energies. This is known as spin-orbit splitting[59].

$$j = l \pm s \tag{20}$$

where j is the total angular momentum, l is the orbital quantum number and s is the spin (s $= \pm\frac{1}{2}$). Suppose an electron in the first excited state (n = 2 and l = 1)., substituting this in to equation (20) we see j will be 1/2 and 3/2 and the ratio of these peaks will be $2p_{1/2} : 2p_{3/2} = 1:2$. This is true for higher values of n, see below.

Table 7. Peak ratios of doublet peaks at higher values of n. [60].

n	Sub-shell	j values	Area ratio
1	s	1/2	n/a
2	p	1/2 3/2	1:2
3	d	3/2 5/2	2:3
4	f	5/2 7/2	3:4

The intensity of the resultant peaks i.e. the number of electrons detected, is proportional to the number of surface atoms and thus makes a useful tool in measuring stoichiometry of a sample. By comparing the intensities and the Full width Half Maximum (FWHM) the elemental composition of Cl-doped perovskite as well as the stoichiometry will be determined. The FWHM will also provide clues into chemical state changes and physical influences in the sample such as broadening due to beam damage or contaminants.

6.12 X-ray Diffraction (XRD)

XRD was performed on the Bruker D8 (Bragg-Brentano geometry, Cu $K\alpha$) and samples were run between $10°$ and $60°$ 2θ with a step size of $0.04°$ and a step time of 0.5 s.

XRD is a analytical technique that is able to extract structural information about a sample such as lattice parameters and space group. Below is an illustration of a Bragg-Brentano XRD.
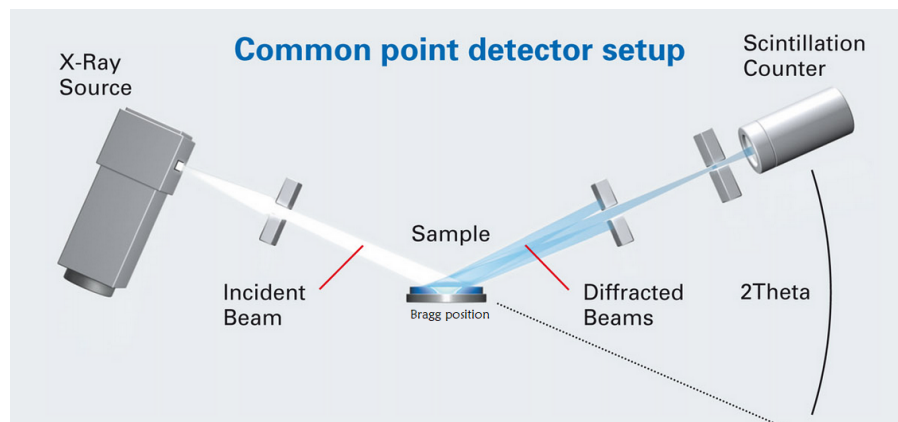
Figure 14. Illustration of XRD exhibiting Bragg-Brentano geometry.[61]

A sample is placed in Bragg position (figure 14) and X-rays are generated via thermal liberation of electrons that are then accelerated and directed through a potential difference of 30 kV and collide with a rotating anode, often made of copper. The bombardment of thermal electrons excite the electrons within the copper to higher energy levels and upon relaxation emit X-rays of characteristic ra-

diation (Cu $K\alpha = 1.5406\mathring{A}$) [62].
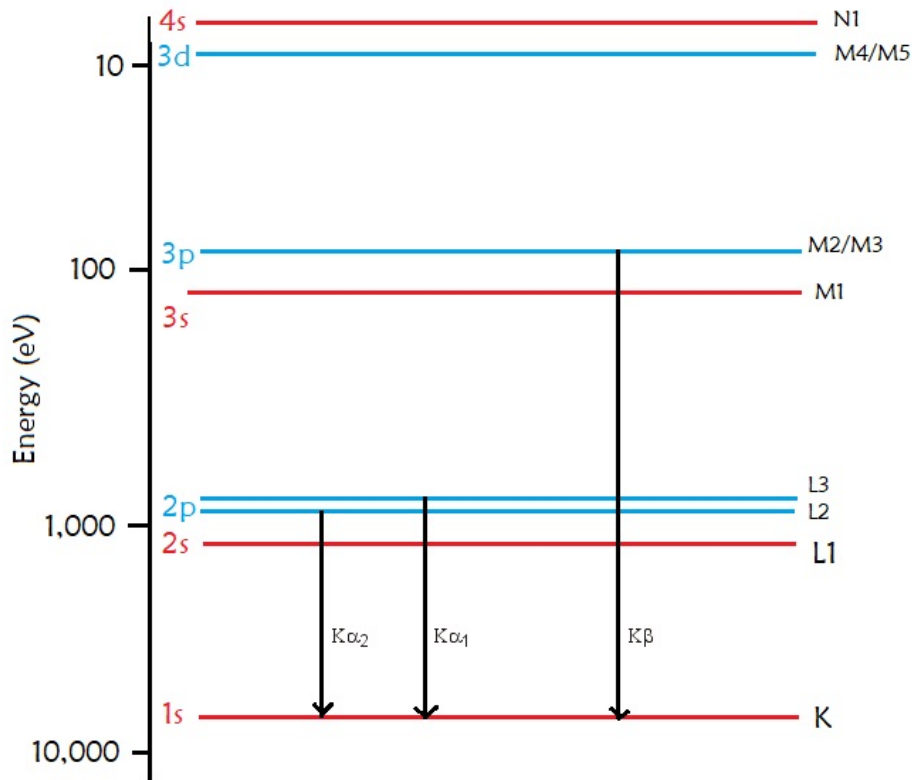
Figure 15. Illustration of X-ray generation from allowed electron transitions in copper.

The origin of Kα radiation arises due to the splitting of energy levels into multiple allowed states (as seen in the figure above), the small differences in energy yields the generation of photons with slightly different wavelengths. Cu Kα_2 = 1.5411 $\mathring{A}$.

6.12.1 Diffraction

A diffraction peak will be observed when the incident X-rays ($\vec{K_0}$) interact with a crystal lattice and constructively interfere with the scattered X-rays ($\vec{K'}$). With the aid of an illustration (below) an expression for constructive interference can be formed:
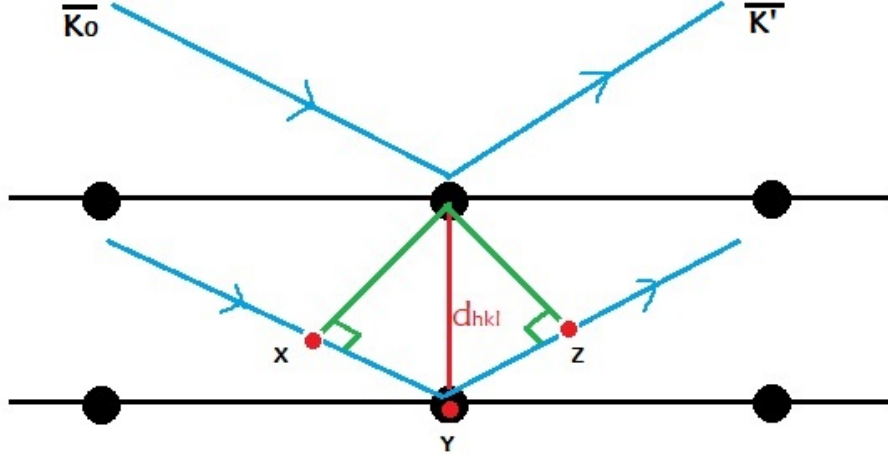
Figure 16. Illustration of incident X-rays (K_0) interacting with a lattice and scattering elastically as k'. Where d_{hkl} is the interplanar distance.

Trigonometry can be used to find an expression for the path distances from point 'X' to point 'Y' and from 'Y' to 'Z'

$$XY = d_{hkl}Sin(\theta) \tag{21}$$

and

$$YZ = d_{hkl}Sin(\theta) \tag{22}$$

The condition for constructive interference must be an integer value and a multiple of the initial wavelength: $n\lambda$

Thus,

$$XY + YZ = n\lambda \tag{23}$$

$$2d_{hkl}Sin(\theta) = n\lambda \tag{24}$$

The superposed waves are then detected by the instrument and a diffractogram is produced. With a known wavelength and 2θ position, information regarding the lattice parameters, space group and crystallite size can be extracted.

6.13   SEM and EDX

Scanning Electron Microsocpy (SEM) and Energy Dispersive X-ray Spectroscopy (EDX) is often used to image the sample's surface

and evaluate its morphology. SEM uses electrons liberated (under vacuum) via thermionic emission, similar to other X-ray techniques, which are accelerated through a potential difference (from 0.5 kV to 30 kV) and guided using a series of magnetic lenses and other optical systems. The electrons then scan over the surface of the sample, producing secondary electrons, back-scattered electrons and X-rays characteristic of the elements within the sample. The table below summarises the above.

Table 8. summary of electron interactions.

Electrons	Comment
Back-scattered	A fraction of incident primary electrons are reflected back towards source
Secondary	Originate from deeper within the sample, less energy - less resolution
X-rays	Elemental composition of the sample

As core electrons are ejected out of the material, outer-shell electrons fill the new core vacancies and emit X-rays. The X-rays are then detected by a spectrometer inside the instrument that generates a spectrum where the peak position is characteristic of the element(s) in the sample - hence Energy Dispersive X-ray Spectroscopy (EDX).

41

7 Chapter 3

7.1 Precursor Solution

Existing literature and X-ray photo-electron Spectroscopy (XPS) has shown that a molar ratio of 3:1 (MAI:PbX_2) enhances morphology and performance [17] and is widely utilised for the synthesis of MAPI so this is what is used in this study. Methylammonium iodide (Solaronix) and lead iodide (Sigma) were weighed out and the MAI was dissolved in 6 ml of N,N - dimethylformamide (DMF) and allowed to mix using a magnetic stir bar under a nitrogen atmosphere, for 45 minutes before adding the PbI_2 and allowing a further 30 minutes for mixing.

It is worth noting here that $PbCl_2$ was particularly insoluble in DMF, which is suspected to be the primary reason for poor deposition results towards high Cl concentrations. It was later found that a molar mixture (1:1) of DMF:DMSO improved solubility of $PbCl_2$ ad produced high quality chlorine treated perovskite films [63].

The following recipe in table 9 was used to synthesise methylammonium lead iodide perovskite:

Table 9. Illustrating recipe for MAPI.

Ingredient	Molar mass (g/mol)	Calculated mass (g)
Methylammonium Iodide	158.91	0.733
Lead iodide	461.01	0.707

The mass of MAI was provided to be 0.733 g and thus the number of mol can be calculated via the relationship:

$$Number of mols = \frac{M_g}{M_\mu} \tag{25}$$

Where M_g is the mass in grams and M_μ is the accepted value for the molar mass.

$$4.611 mmol = \frac{0.733}{158.97} \tag{26}$$

This then allowed the mass contribution of the PbI_2 to be calculated.

During the mixing, boro-silicate glass (1 mm Corning Eagle) substrates were cut to an arbitrary length (enough to cut up into multiple samples) and cleaned using the procedure mentioned above.

7.2   Deposition

In the early stages of deposition, the tube furnace with quartz insert (see figure 5) was pre-heated to $T = 140°C$ and flushed with nitrogen to dry the atmosphere and remove any solvent vapours. The substrate was inserted into the furnace and allowed to pre-heat before starting the deposition. Once the precursor solution had been transferred from the fume hood to the furnace, the apparatus was connected and secured with plastic clips. A mist was generated using the nebuliser which was allowed to fill the volume of the flask and nitrogen was introduced to the system which directed the precursor mist into the tube furnace. A few modifications to the parameters were made throughout the duration of this study but this will be evident a little later.

During deposition, substrate position proved to be vitally important as a 'goldilocks' zone seemed to exist just outside the hottest region (centre) of the furnace, though this was different depending on the type of perovskite synthesised. Deposition of PbI_2 films were modified to include multiple substrates in different regions of the furnace. It was recorded that a thicker, more uniform film had grown on the substrate towards the exhaust of the system. However, depositing films of perovskite with high $PbCl_2$ concentration showed good film quality when substrate is placed in the centre ($T \approx 150°C$), compared to exhaust point ($T < 140°C$).

7.3   Sample Series'

The following series was the first attempt at depositing MAPI (see appendix for recipes used). Once deposition of the samples was completed, samples were immediately stored in a nitrogen filled glove box until characterisation and a simple colour coded table was generated to separate discarded samples from successful ones, as seen below.

Table 10. Tabulated series summary of samples CGT 1-8. Green corresponds to successful and red corresponds to discarded samples for all tables in this chapter.

Sample	T (°C)	duration (t)	Flow rate (l/min)	Comment	Date
CGT1	140	1 hr	0.3	Film barely covered substrate	23/10/2019
CGT2	160	1.25 hr	0.3	Better, still very thin	24/10/2019
CGT3					
CGT4	160	1 hr	0.4	Poor quality - very thin	24/10/2019
CGT5	140	1 hr	0.3	Solution left overnight under N2	24/10/2019
CGT6	140	1 hr	0.3	Better coverage, still thin	24/10/2019
CGT7					
CGT8	160	1.3 hr	0.4	Best so far!	29/10/2019

In hindsight, it is clear that an increased duration and temperature than initially trialed produced the most successful samples. The extended duration produced visually darker films, indicating the films were thicker than the translucent films.

7.3.1   Steel Susceptor

Due to the fact that only 25% of samples in the first series were successful, some consideration was taken into modifications to improve the resultant film. This led to the use of a susceptor in order to angle the substrate so more area is directly exposed to the incoming material. It quickly became apparent that this is already well utilised within literature, and so was trialled in this study. A steel susceptor was used since a carbon susceptor could not be manufactured. The advantages of using a carbon over a steel suscpetor are the improved thermal properties, chemical inertness of carbon and resistance to chemical attack from solvent vapours. It is also worth noting that from this point on a different furnace was used throughout this study and a quick calibration showed less of a temperature gradient and thus more uniform heating (see appendix).

Table 11. tabulated series summary of samples CGS 1-6.

Sample	T (°C)	duration (t)	Flow rate (l/min)	Comment	Date
CGS1	160	1 hr	0.3	Solution carried over	12/11/2019
CGS2	150	1 hr	0.4	Reddish band on edge	14/11/2019
CGS3	160	1 hr	0.3	PK deposited well on susceptor	12/11/2019
CGS4	150	1 hr	0.4		14/11/2019
Sample	T (°C)	duration (t)	Flow rate (l/min)	Comment	Date
CGS5	150	1 hr	0.3	Nice coverage, beautiful red colour!	18/11/2019
CGS6	150	50 min	0.3	Similar results to S5	19/11/2019

Summarised in the table above are the parameters of deposition and a comment of the resultant film. CGS2 exhibited a reddish band on the edge of the substrate and the only thing different in this experiment was the inclusion of the steel susceptor. This was investigated further to see if the red colour could be reproduced in CGS5 and the picture below captured what was achieved.

Figure 17. Freshly deposited CGS5 exhibiting a beautiful red colour. Approx dimensions = 7cm x 2cm.

More details regarding the red colour will be elaborated upon later in this thesis.

7.3.2 Without Susceptor

Following the results of the CGS series, an identical solution was used to run two more samples, this time without the susceptor to see whether or not a red colour would be present, table 12 below summarises the series.

Table 12. Summary of CGWOS series.

Sample	T (°C)	duration (t)	Flow rate (l/min)	Comment	Date
CGWOS1	150	1 hr + 1 hr	0.3	Ok coverage - very thing	14/11/2019
CGWOS2	150	1 hr	0.3	Nebuliser too high (reddish)	14/11/2019

Deposited films were still poor quality and were discarded, so to try and improve this, CGWOS1 was deposited and then put back into the furnace during the deposition of CGWOS2. but this had very little to no effect on CGWOS1.

CGWOS2 did exhibit a slightly red colour but this was attributed to impurities still left in the furnace from the susceptor in the previous series. So, the apparatus was cleaned before running any more experiments which removed red colouration from samples.

7.3.3 Steel Substrate

Due to the initial observation that material had deposited on the susceptor and adhered quite well, a series using steel substrates was investigated.

Table 13. Summary of CGSS series (steel susceptor).

Sample	T (°C)	duration (t)	Flow rate (l/min)	Comment	Date
CGSS1	150	1 hr	0.3	Poor quality - no adhesion to substrate	18/11/2019
CGSS2	150	1.5 hr	0.3	Discarded	18/11/2019
CGSS3	150	1.5 hr	0.3	Discarded	18/11/2019
CGSS4	150	1 hr	0.3	Discarded	18/11/2019

As we can see from the table, the results were very poor and the whole series was abandoned.

7.3.4 Thicker Film

The thickness of a sample can be judged by eye by gauging the translucency of the film and suspicions of thin films were confirmed via SEM. After experimenting with apparatus and achieving poor results, efforts were concentrated on procedure and synthesis of thicker MAPI films. The reaction duration was set to t=1.5 hr to allow more material to be deposited, this however, was not long enough and the time was extended to 2 hours.

Table 14. Showing various substrates (CE, titania and FTO) were used in this series and two samples of each substrate were prepared.

Sample	T (°C)	duration (t)	Flow rate (l/min)	Comment	Date
CETF1	150	1 hr 10 min	0.3	Nice coverage - thin (allow to decay)	19/12/2019
CETF2	150	1.5 hr	0.3	Turbulent deposition (discard)	19/12/2019
TiTF1	150	1.5 hr	0.3	Darker / thicker film	19/12/2019
TiTF2	156	1 hr	0.3	Thin coverage	19/12/2019
FTOTF1	150	1.5 hr	0.3	Difficulty generating precursor mist	19/12/2019
FTOTF2	150	1 hr 10 min	0.3	Nice, uniform coverage	19/12/2019

A visual inspection of substrates suggests the cleaning method influenced coverage and that duration needed to be extended. The resultant films yielded better coverage and were visibly darker than previous attempts.

7.3.5 Long Duration

Following the observations of the previous series, (thicker film) deposition duration was increased in an attempt to improve film results. Observations of the films after deposition appeared darker than previous samples and this was confirmed by transmission and reflection measurements (see results). The improved thickness was attributed to the reaction duration and the rate of nebulisation.

Table 15. Illustration of the accepted and rejected samples synthesised in this series.

Sample	T (°C)	duration (t)	Flow rate (l/min)	Comment	Date
CELD1	150	2 hr	0.4	Darker looking film	09/01/2020
TiLD1	150	1.5 hr	0.4	Flask broke - destined to fail!	09/01/2020
TiLD2	150	2 hr	0.4	Turbulent - looks ticker/darker	10/01/2020
FTOLD1	150	2 hr	0.4	Better deposit closer to inlet	10/01/2020
CELD2	150				
FTOLD2	150	2 hr	0.4	Thinner closer to inlet	22/01/2020

All things considered, the substrate did not have significant effect on the resultant film quality, thus titania and FTO coated substrates were abandoned and CE glass was pursued. The reaction duration, set point deposition temperature and the flow rate were considered to be optimised as previous series' saw that temperatures around 160°C produced poor results and an increased reaction duration generally improved film quality. A flow rate of 0.4 l/min was used, as any higher would result in loss of solution that would condense in the cold end of the furnace.

47

7.4 Chlorine doped MAPI $CH_3NH_3PbI_{3-x}Cl_x$

To introduce Cl-doped samples, the mass of each component was calculated as before.

Table 16.

Mass contributions of constituents following stoichiometry $CH_3NH_3PbI_{3-x}Cl_x$.

Sample	$PbCl_2$	PbI_2	$PbCl_{2\ (mmol)}$	$PbI_{2\ (mmol)}$	$PbCl_{2\ (g)}$	$PbI_{2\ (g)}$
1	0	1.0	0	1.537	0	0.709
2	0.1	0.9	0.154	1.383	0.043	0.638
3	0.3	0.7	0.461	1.076	0.128	0.496
4	0.5	0.5	0.768	0.768	0.214	0.354
5	0.7	0.3	1.076	0.461	0.299	0.213
6	1.0	0	1.537	0	0.427	0

The highest quality samples were synthesised at a set point deposition temperature of 150°C, a reaction duration of 2 hours and a nitrogen flow of 0.4 l/min. So these were the parameters selected for the chlorine doped series.

Table 17. Displaying sample concentration Cl : I and the parameters for deposition. In order to assess the influence of chlorine in the perovskite samples, all samples were characterised.

Sample Cl:I	$T(°C)$	Duration	Flow rate (l/min)
0.0 : 1.0	150	2hr	0.4
0.1 : 0.9	150	2hr	0.4
0.3 : 0.7	150	2hr	0.4
0.5 : 0.5	150	2hr	0.4
0.7 : 0.3	150	2hr	0.4
1.0 : 0.0	150	2hr	0.4

8 Chapter 4

8.1 Results and Discussion

8.1.1 UV Treatment of TiO_2 Surfaces

Improving the wettablity of substrates leads to improvements in surface coverage, due to a reduced contact angle between the liquid precursor drop and the substrate surface. This allows the liquid to spread across the surface, resulting in better coverage and enhanced uniformity.

For this investigation 10 μl of solvent (DMF and DMSO) were added to an un-treated substrate (glass, titania and FTO) and the diameter of the drop was recorded using a vernier caliper. All substrates were exposed to 15 minutes of UV radiation ($\lambda = 350nm$, approx 20 mW/cm^2) and the procedure was repeated. Once the diameters of each drop were taken, the contact angle of the drop with the substrate can be calculated.
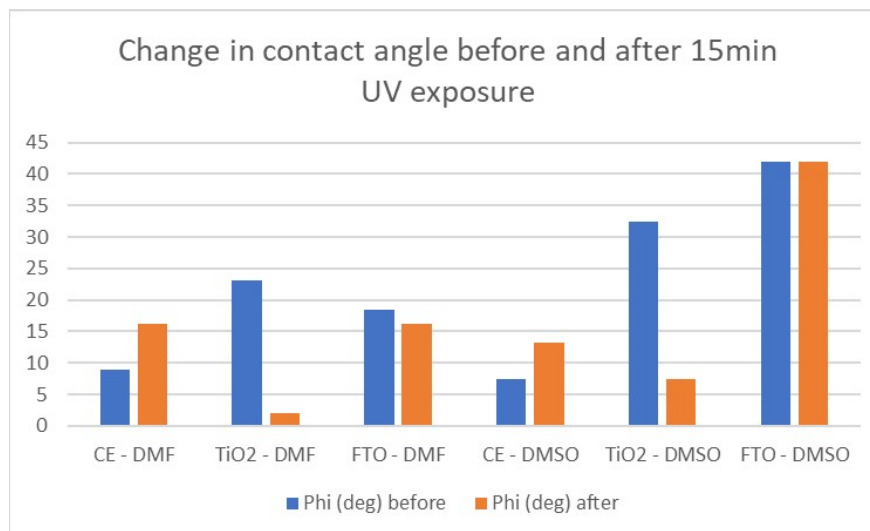

Figure 18. Graph of contact angle before and after 15 minutes of UV treatment.

As we can see, there is no significant change to the contact angle as a result of UV exposure for the FTO substrates and apparently produced a slight hydrophobic effect in the uncoated CE substrates.

Titania coated substrates show a drastic change as expected.

It was quickly realised that the hydrophilicity of the titania coated substrates was very time sensitive and lasted no longer than 15 minutes. A plot of hydrophilicity against time is shown below.
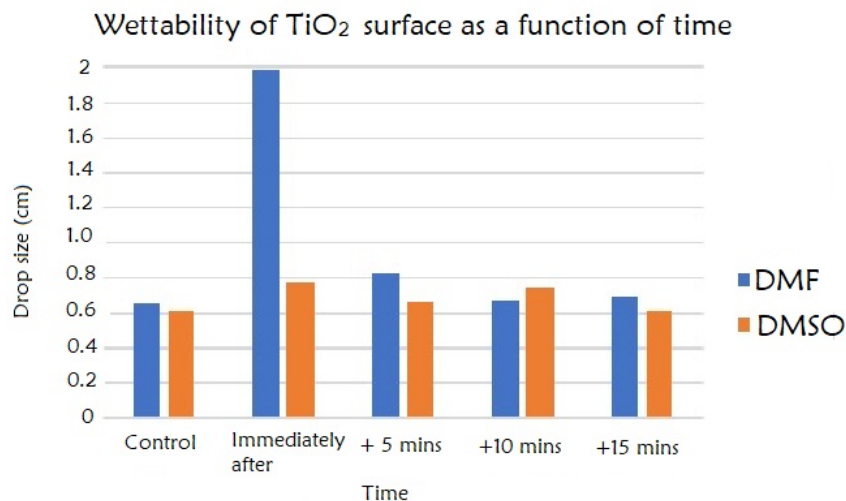

Figure 19. A graph of the wettability of titania surface as a function of time.

From these data, a remarkable change in drop size with DMF solvent, deposited on titania, immediately after UV exposure is clearly evident, so titania coated substrates were employed for a duration of this study in an attempt to improve surface coverage.
Successful samples were kept and stored in a dry glove box until further characterisation. Below, in table 17 is a summary of successful samples.

Table 17.

Sample	deposition temperature	Duration (t)	comment
CGT2	160	1.25 hr	Poor quality
CGT8	160	1.30 hr	Improved quality
CGS2	150	1 hr	Exhibited slight reddish band
CGS5	150	1 hr	Beautiful red colour
CGS6	150	50 min	Slight red colour
Cl series	150	2 hr	

Further characterisation on successful samples (table 12) involve UV-Vis, PL, XPS and X-ray Fluorescence Spectroscopy (XRF). However, analysis using Time Resolved PL, XRD and SEM were detrimentally impacted due to global pandemic COVID-19 and closure of university facilities (18/03/20 - 04/08/20).

8.2 Optical Characterisation

8.2.1 Samples T2 - T8

UV-VIS measurements were taken on an Aquila NKD 8000 spectrophotometer, P-polarised, glancing angle $= 30°$ between the range of 400 nm - 1100 nm. See figure 26:
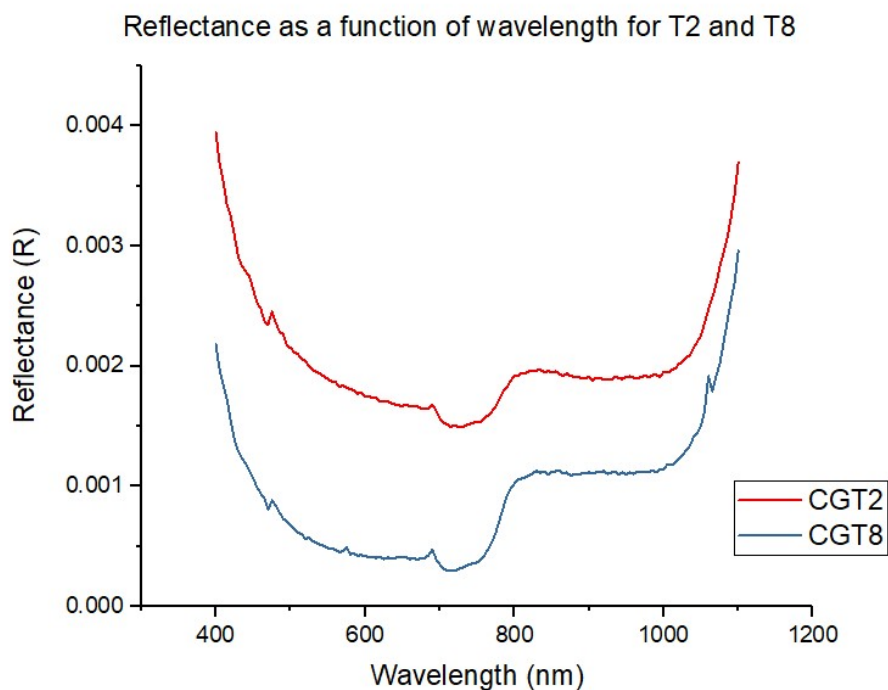

Figure 20. Reflection measurements for initial samples T2 and T8.

Methylammonium lead iodide perovskite exhibits an optical feature in the form of an absorption edge in the vicinity of the band gap energy as evidenced in Figure 21. The reported absorption edge for $CH_3NH_3PbI_3$ is approximately 760 nm corresponding to an energy gap of around 1.50 eV [64] consistent with figure 20. UV-VIS measurements can be used to estimate the band gap energy using a Tauc

relation $(\alpha h \nu)^2$ (See figure 21). However, there is debate regarding the significance of the estimation, since it is prone to cognitive bias. The x-intercept provided by the plot depends on the gradient and thus the x-intercept can be 'selected' to best support the case being made.
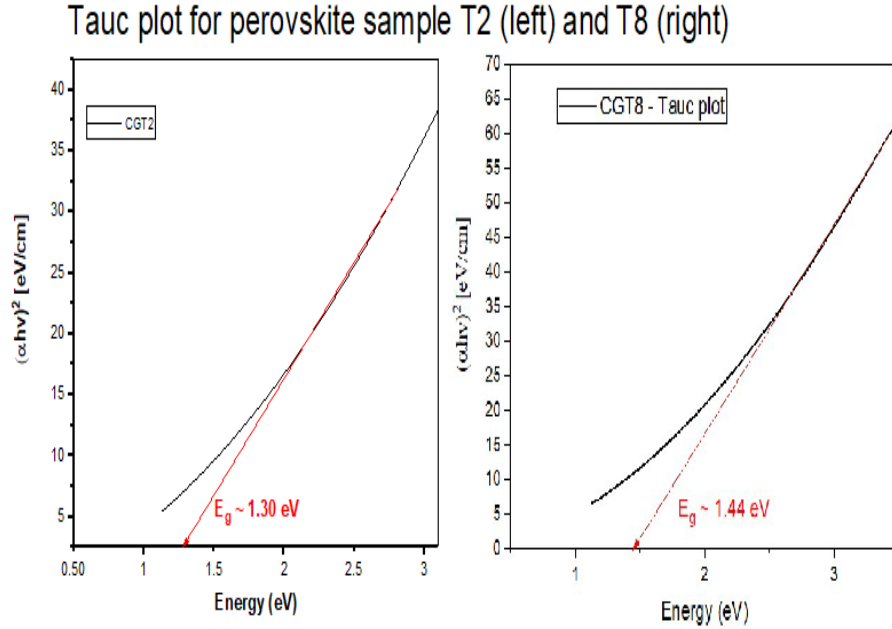

Figure 21. Tauc plots of perovskite samples T2 and T8, with estimated band gap.

The band gap determined via Tauc relation in figure 21 is in reasonable agreement with literature, however more precise band gap measurements were taken using PL. The discrepancies in band gap energy could be due to the formation of non-target chemical species such as PbI_2 and other impurities in the film.
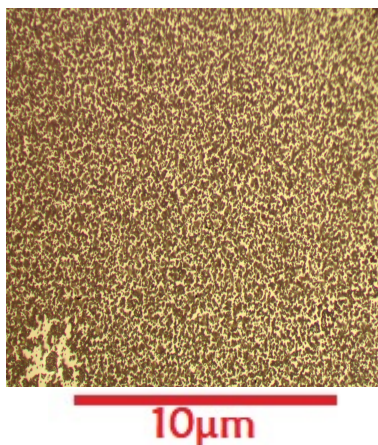
Figure 22. Optical microscopy of initial sample T2, showing a poly-form film and island formation of perovskite.

Sample T2 as seen in figure 22 resulted in a somewhat powdery deposit, which has previously been reported using AACVD [44]. A set point deposition temperature of $160°C$ was used and ultrasonic humidifier was set to max, this seemingly resulted in a notably faster deposit at the expense of film quality.

8.2.2 Samples S2 - S6

In this sample series, the 'S' denotes the use of a steel susceptor and was used in order to directly expose more substrate area to the precursor flow. A reduced deposition temperature of $150°C$ was used for the duration of an hour. Sample S2 exhibited a very slight red tint to the film (see next page).
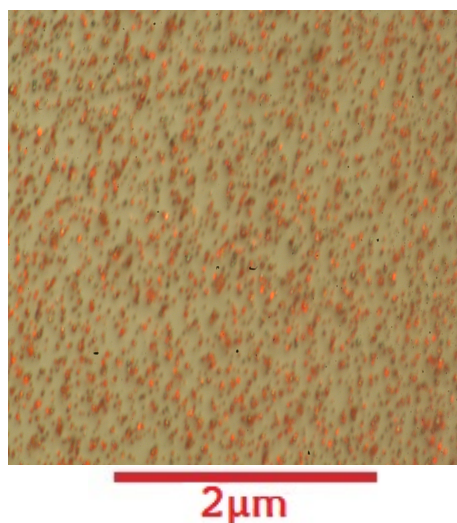
Figure 23. Shows sample S2 under 50x magnification exhibiting red crystals.

The only modification to the process that could have been responsible for this result was the use of the susceptor so, two more samples S5 and S6 were prepared in an attempt to recreate the red colour. Below is an image of sample S5 regarded as the most successful attempt to reproduce red colouration.

Figure 24. Sample CGS5 exhibiting beautiful red colour. Approx dimensions = 7cm x 2cm.

Figure 25. Sample S6 removed from furnace early as solution had depleted. Distinct regions of varying stages of formation are observable with black being perovskite and off-white being PbI_2. Red region still unidentified. Approx dimensions = 7cm x 2cm.

Three successful runs in reproducing the red colour attributed to potential iron (Fe) doping from the susceptor. It is worth noting that the red regions are far more sensitive to degradation in air than perovskite, decaying and losing colour within an hour or half an hour in some cases. Further PL measurements were taken in order to see if there was any optoelectronic influence due to doping.
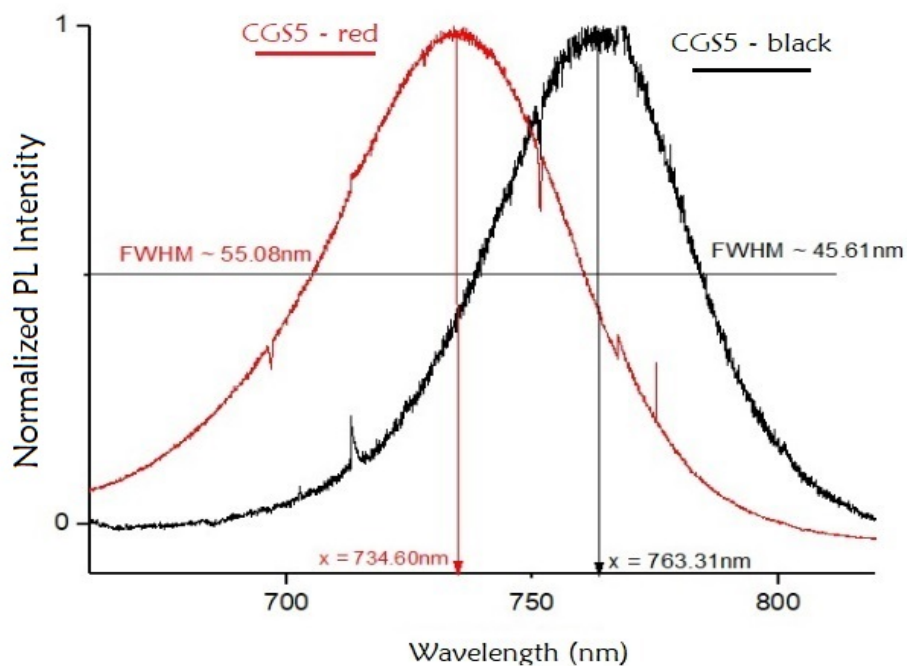
Figure 26. Sample S5 showing the PL response from each region for sample S5. Band gaps calculated to be, red = 1.69 eV and black = 1.62 eV.

With optoelectronic influence confirmed, efforts were concentrated on determining the elemental composition of the black and red regions. A broader FWHM exhibited by the red region further suggest some increased level of impurities. X-ray Fluorescence (XRF) was performed on sample S5 to determine elemental composition. However, XRF does not provide any information on the oxidation states, for this, XPS would be required.
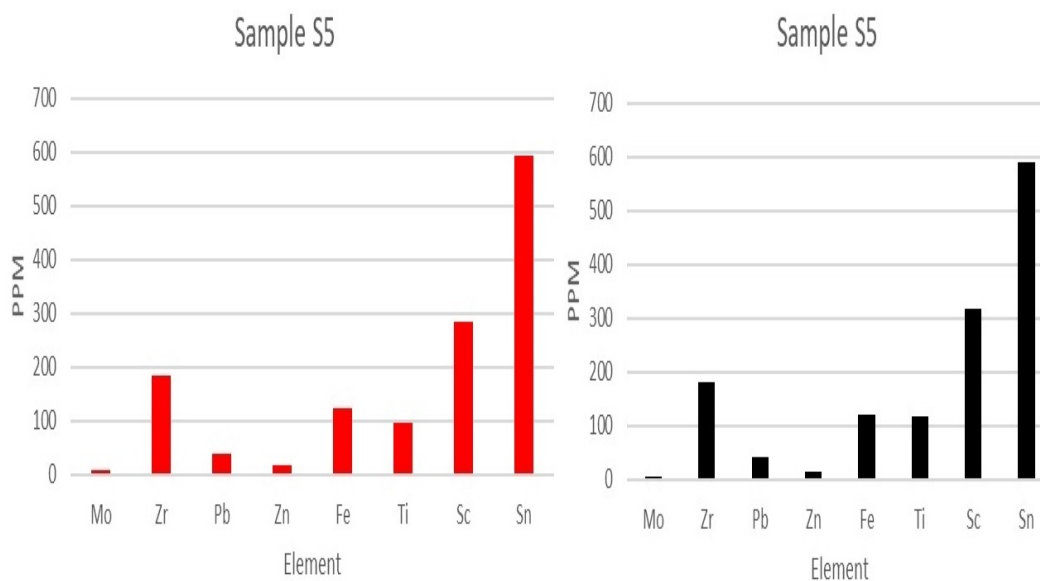
Figure 27. Shows elemental composition in PPM of the red region (left) and black region (right) of sample S5. Almost identical composition, strontium and calcium have been omitted from this figure due to high concentrations of these elements within the glass substrate.

Both regions show a very similar composition, challenging the initial idea that the red colour was attributed to iron doping. A more precise determination of elemental composition using XPS would have been the preferred method, so a red sample was synthesised for XPS. Unfortunately, the sample had decayed and lost its red colour during the packaging process and could not be used for XPS.

8.3 $CH_3NH_3PbI_{3-x}Cl_x$ Characterisation

To first explore the optoelectronic properties of Cl doped perovskite thin films, UV-VIS spectroscopy was performed.
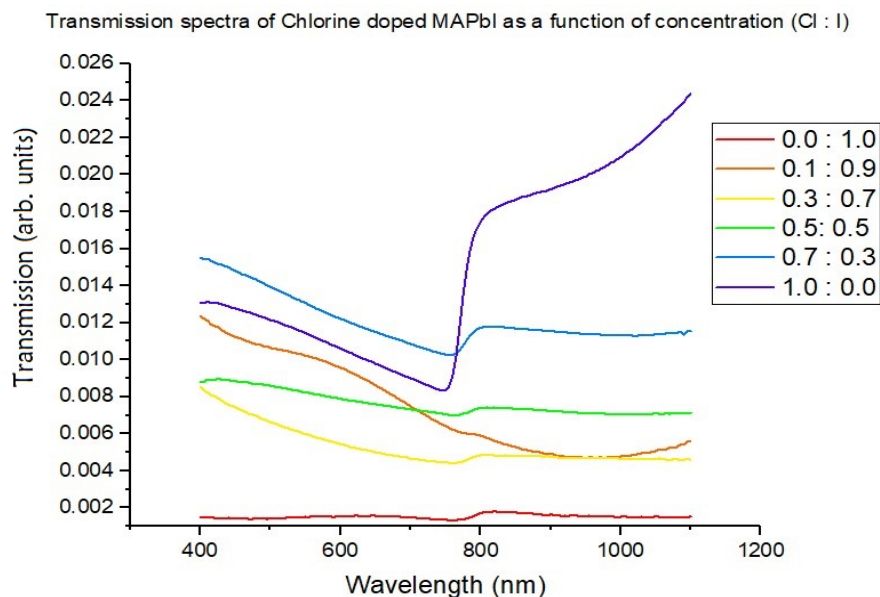
Figure 28. Shows the transmission spectra for chlorine treated perovskite samples exhibit a sharp optical feature associated with the band gap transition. Changes in magnitude, gradient and position as a function of chemical composition confirm some optoelectronic influence due to the presence of chlorine. Red = low concentration, blue = high concentration.

As we can see from figure 28 the sharpest absorption edge belongs to X = 1.0 concentration, this is attributed to freshness of the sample since perovskite readily degrades in ambient air. Although, it has been shown that Cl incorporation also influences morphology[35] and morphologically pristine films should exhibit sharper, more intense optical signatures due to the absence of pin holes and defects that affect recombination and film performance.

For concentrations less than X = 0.5, a relatively small absorption edge is apparent, suggesting sample degradation due to age. Samples were synthesised and analysed in order of increasing concentration over the course of 5 days. Photoluminescence spectroscopy yields a more accurate determination of band gap by extracting the peak wavelength, see next page.
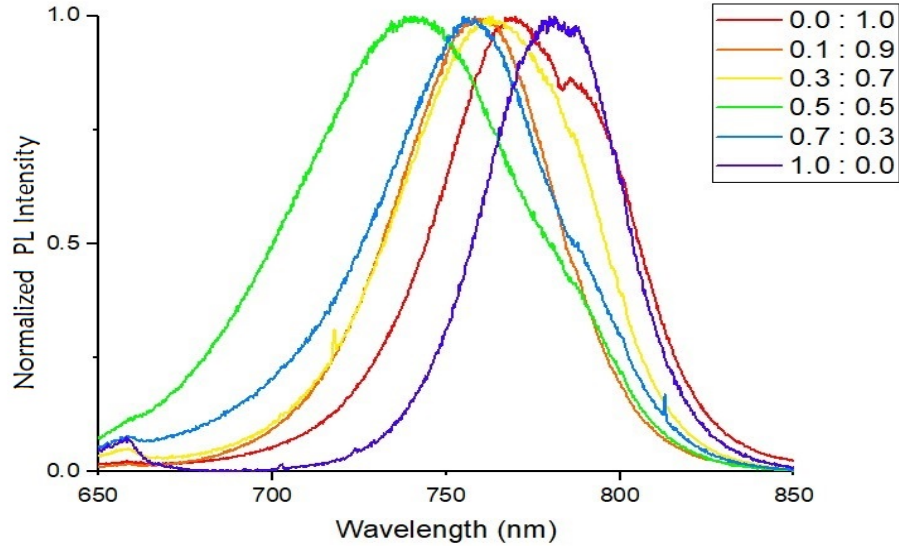
Figure 29. Shows the normalised PL response for this chemical series as a function of increasing chlorine concentration. Red = low concentration, blue = high concentration.

Upon closer inspection, doped samples of increasing concentration exhibit an anti-Stoke shift towards higher band gap energies up until a concentration of 0.5 : 0.5 (Cl : I), while above X = 0.5 concentration, the PL peak exhibits a Stokes shift towards lower band gap energies. Previous studies have observed similar behaviours of perovskite due to halide substitution[39]. A more precise study investigating concentrations between X = 0.5 and X = 1 should be undertaken in order to clarify this behaviour.

Table 18. Illustrates more clearly the experimentally determined electronic properties of chlorine treated perovskite films. Confirming optoelectronic influence due to the presence of chlorine.

Concentration (Cl : I)	Peak wavelength (nm)	Energy gap (eV)	FWHM (nm)
0.0 : 1.0	769.85	1.61	60.91
0.1 : 0.9	758.27	1.64	52.05
0.3 : 0.7	762.39	1.63	63.59
0.5 : 0.5	739.68	1.68	79.34
0.7 : 0.3	754.92	1.64	61.09
1.0 : 0.0	779.62	1.59	46.47

There is distinct variation in FWHM suggesting varying levels of purity of samples, including indication of dopant level, crystallinity - larger crystallites mean less grain boundaries and therefore, less trap states. PL signal from non-target chemical species is often contained inside the main peak, which can lead to broadening. A large FWHM implies there are more impurities and defects in the sample compared to a low FWHM. From table 13 we can see that concentration $X = 0.5$ possess the broadest peak and $X = 1.0$ possess the narrowest and while some degree is attributed to freshness and age of the sample ($X = 1.0$ fresher than $X = 0.5$) there may be competition between iodine and chlorine incorporation. To confirm whether changes in FWHM were due to age or halide dopant level, samples were anlaysed using XPS.

8.4 XPS measurements

X-ray Photoelectron Spectroscopy (XPS) was performed on a Thermo Fisher Scientific K-alpha spectrometer. Samples were analysed using a micro-focused monochromatic Al X-ray source (72 W) over an area of approximately 400 microns. Data was recorded at pass energies of 200 eV for survey scans and 40 eV for high resolution scan with 1 eV and 0.1 eV step sizes respectively. Scans were performed both before and after a 30 s (4 keV) argon etch to remove any surface contaminants. Charge neutralisation of the sample was achieved using a combination of both low energy electrons and conductive tape.

Five samples of varying Cl concentration were analysed using XPS to determine the surface and sub-surface elemental composition of Cl doped perovskite $CH_3NH_3PbI_{3-x}Cl_x$ [X = 0, 0.1, 0.5, 0.7 and 1.0]. The samples were stored in the glove box until packaging where they were all exposed to air for a small period of time. Samples were placed in rectangular boxes and held in place via adhesive. The sample boxes were then vacuum packed and double sealed before shipping, in order to avoid ambient contamination.
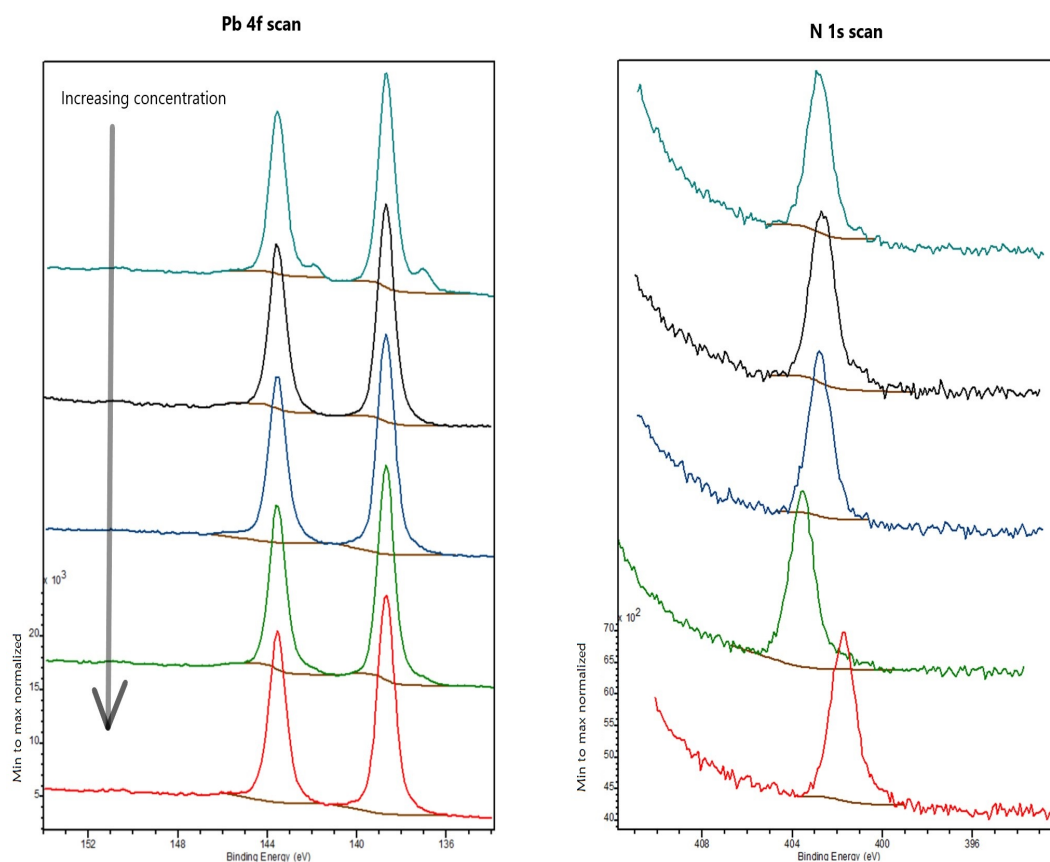

Figure 30. (left) shows Pb $4f_{7/2}$ peak situated at 138.7 eV associated with perovskite and was used for calibration. A small shoulder can be observed in low concentration sample attributed to metallic lead. Figure 31. (right) shows N 1s scan corresponding to methylammonium cation at 402.7 eV.

Each scan confirmed the presence of Pb, I, N, and C consistent with perovskite but also the presence of an O 1s signal at 533.2 eV which is typically associated with water absorbed via exposure to humidity[65]. The presence of this signal didn't change significantly upon sputtering which could reflect the samples age/exposure time, so the level of oxygen is not due to further degradation during transport. No samples including sputtered show presence of Cl even at maximum Cl concentration (1:0) though this is in good agreement with literature[35] [36]. Zhou et al reported no detectable levels of Cl in samples and only a very weak signal in another which was also consistent with Xie et al, reporting mixed success obtaining a very weak Cl 2p signal occurring at 198.9 eV and 200.5 eV for the $2p_{3/2}$ and $2p_{1/2}$ peaks, respectively in the top 20 nm of the sample.

A strong C 1s signal corresponding to MA cation at 286.78 eV was present, consistent with literature[66] although a weaker C 1s signal at 285.2 eV relating to amorphous carbon was also present – impurity due to handling. A N 1s surface impurity was also detected at 400.2 eV attributed to an amine group and main peak corresponding to perovskite at 401.7 eV consistent with 401.5 eV reported by Zhou et al [67] and Yates et al[65].

However, sputtered data show a slight reduction in N 1s and I 3d peaks at greater sample depths. I 3d doublet present at 630.2 eV (3/2) and 618.6 eV (5/2) $\Delta E = 11.6$ eV differs by 0.5 eV according to literature[65]. In all samples strong $Pb4f_{5/2}$ and 7/2 signal at 143.5 eV and 138.7 eV, respectively consistent with PK and a weak signal at 137.2 eV assigned to metallic Pb. Metallic Pb signal increased after sputtering consistent with previous perovskite XPS studies [65]. This is often ascribed to beam damage.

Table 19. Summary of peak positions compared with literature.

Element	My peak (eV)	Literature value (eV)	Auhor
C 1s	286.78	286.41	Zou
N 1s	401.7	401.5	Yates
I 3d	(3/2) 630.2	630	Yates
Pb 4f	(7/2) 138.7	138.7	Yates

.

Table 20. Illustrating stoichiometry determined by XPS measurements prior to sputtering.

Concentration (Cl : I)	C	I	N	Pb
0.0 : 1.0	2.40	2.04	1.07	1
0.1 : 0.9	1.32	1.24	0.64	1
0.5 : 0.5	1.74	1.9	1	1
0.7 : 0.3	2.21	1.93	1.17	1
1.0 : 0.0	2.64	1.82	1.06	1

Table 21. Illustrating stoichiometry after 30 s argon sputtering.

Concentration (Cl : I)	C	I	N	Pb
0.0 : 1.0	2.59	2.05	1.45	1
0.1 : 0.9	1.81	1.75	0.82	1
0.5 : 0.5	1.55	1.81	0.91	1
0.7 : 0.3	2.47	2.54	1.02	1
1.0 : 0.0	2.32	1.73	0.95	1

Compared to the ideal ratio 1:3:1:1 (C:I:N:Pb) these results are in poor agreement. This could be attributed to the time between deposition and performing XPS. Carbon contamination seems high even after sputtering, suggesting contamination of bulk material. No easily identifiable pattern in the amount of iodine, as it was expected that I to remain roughly the same and reduce slightly as Cl concentration increases. High nitrogen impurity in [0:1] and would have expected N to decrease after etching in accordance with Br-doped perovskite XPS[39]. The significant deviation of results in general from the ideal 1:3:1:1 could be due to sample quality, age, purity or in the process of determining stoichiometry (peak fitting).

8.5   XPS Re-scan

XPS was performed a second time on the same set of five samples and the data was used to investigate the degradation of the perovsktie samples. XPS Analysis was performed using a Thermo NEXSA XPS fitted with a monochromated Al k X-ray source (1486.7 eV), a spherical sector analyser and 3 multichannel resistive plate, 128 channel delay line detectors. All data was recorded at 19.2 W and an X-ray beam size of 200 x 100 m. Survey scans were recorded at a pass energy of 160 eV, and high-resolution scans recorded at a pass energy of 20 eV. Electronic charge neutralization was achieved

using a Dual-beam low-energy electron/ion source (Thermo Scientific FG-03). Ion gun current = 150 A. Ion gun voltage = 45 V. All sample data was recorded at a pressure below 10^{-8} Torr and a room temperature of 294 K.

The same five samples of varying Cl concentration were analysed using XPS to determine the surface and sub-surface elemental composition of Cl doped perovskite $CH_3NH_3PbI_{3-x}Cl_x$ [X =0, 0.1, 0.5, 0.7 and 1.0]. Each sample as before confirmed the presence of Pb, I, N, and C consistent with perovskite. The presence of O 1s signal at 533.2 eV (absorbed water) was still present in all samples. As expected, there was no detection of Cl 2p signal consistent with previous scan and literature.

Table 22. Illustrating the difference in elemental composition of the initial XPS can performed by Harwell on 25/02/20 compared to the rescan also performed by Harwell on 14/07/20.

25/02/20 Initial scan					14/07/20 Re-scan				
Concentration [Cl:I]	C	I	N	Pb	Concentration [Cl:I]	C	I	N	Pb
0:1	2.40	2.04	1.07	1	0:1	2.17	1.54	0.85	1
0.1:0.9	1.32	1.24	0.64	1	0.1:0.9	1.80	0.95	0.68	1
0.5:0.5	1.74	1.9	1	1	0.5:0.5	3.61	1.88	1.54	1
0.7:0.3	2.21	1.93	1.17	1	0.7:0.3	0.98	0.97	0.42	1
1:0	2.64	1.82	1.06	1	1:0	1.38	0.83	0	1

Generally, for all concentrations the elemental presence has decreased aside from a few exceptions. Concentrations of carbon have increased for X = 0.1 and 0.5 suggesting that further contamination of samples due to handling and/or regions on the sample possess local stoichiometries, yielding slightly different concentrations of carbon.

As expected, samples have deviated further from the ideal ratio 1:3:1:1 (C:I:N:Pb) as a result of degradation. Though, atomic fractions of carbon in sample S3 seem unusually high which suggests the region surveyed could have been exceptionally contaminated as

a result of handling. Interestingly, the sample with the highest Cl concentration (X = 1.0) demonstrated the absence of the N 1s signal associated to the methylammonium cation suggesting no perovskite is present in the sample (see figure below).
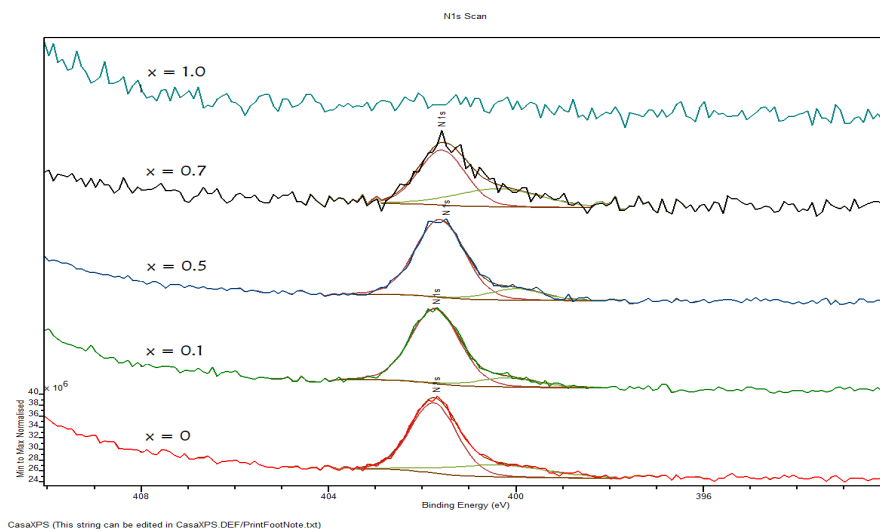

Figure 32. Showing absence of N 1s signal for highest concentration X = 1.0 - 14/07/20 re-scan.

However, XPS survey confirmed the presence of C 1s at 285.7 eV also associated with the methylammonium cation, suggesting perovskite is still present in the sample.
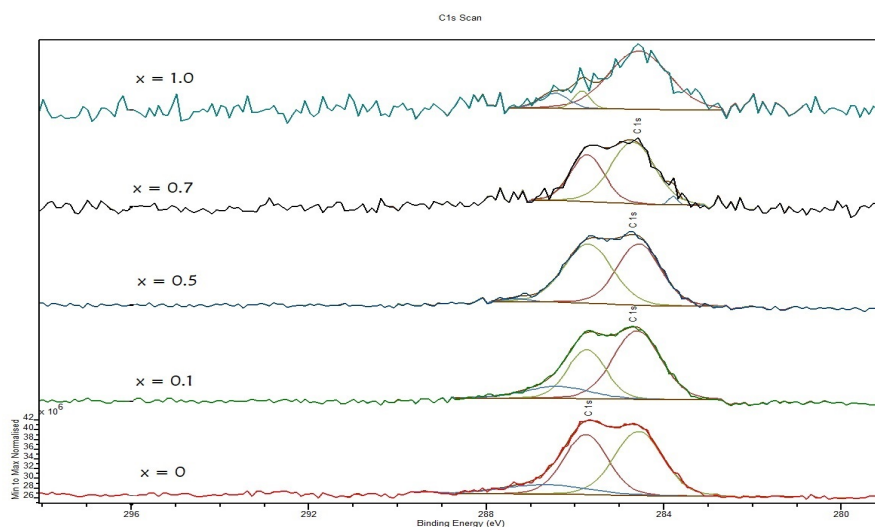
Figure 33. 14/07/20 re-scan showing presence of C 1s peak at 285.7eV, confirming presence of perovskite.

Due to the amine group being absent but the methylammonium group present suggests a local stoichiometry is present in the samples, with regions at various stages of decay. Also, as discussed previously only small amounts of Cl can successfully incorporate into perovskite, higher concentrations introduce instability.

As a result of decay, it is expected that as perovskite degrades into PbX_2 compounds (X = I, Cl, Br), further degradation of PbX_2 into metallic Pb should yield an artefact at 137.2eV. However, based on the evidence below, the survey shows this remains largely unchanged, compared to figure 30.
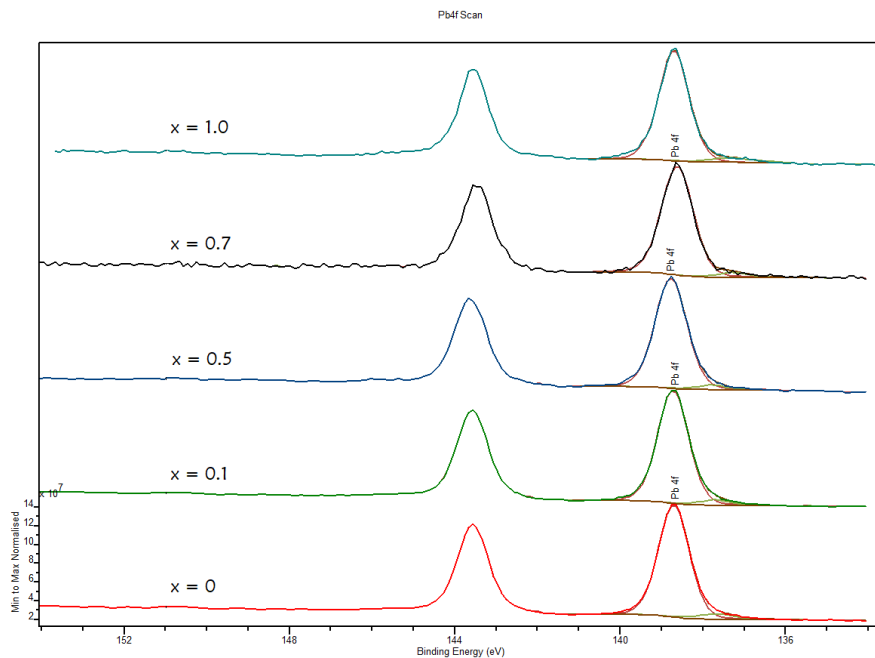
Figure 34. Challenges expectations as no significant change in the main lead $4f_{7/2}$ peak. $Pb_{(o)}$ artefact should have manifested as a small shoulder towards lower binding energies.

8.6   Further XPS

Further XPS investigation was carried out at the University of Manchester as to counter the detrimental impact of COVID-19 to research work. For this a fresh chlorine treated series (named F_Cl), consisting of 7 concentrations was synthesised (X = 0, 0.1, 0.3, 0.5, 0.7, 0.9 and 1.0). Also, to further investigate the influence of halide substitution, two bromine treated samples ($CH_3NH_3PbI_{3-x}Br_x$ [X = 0.5 and 1.0]) were were also use from an older study data of which have been previously reported [39]. No Cl 2p signal was detected though despite their age (approx 2 weeks) weak Br signals were present in the Br treated samples showing storage of samples in glove box delayed decay significantly.
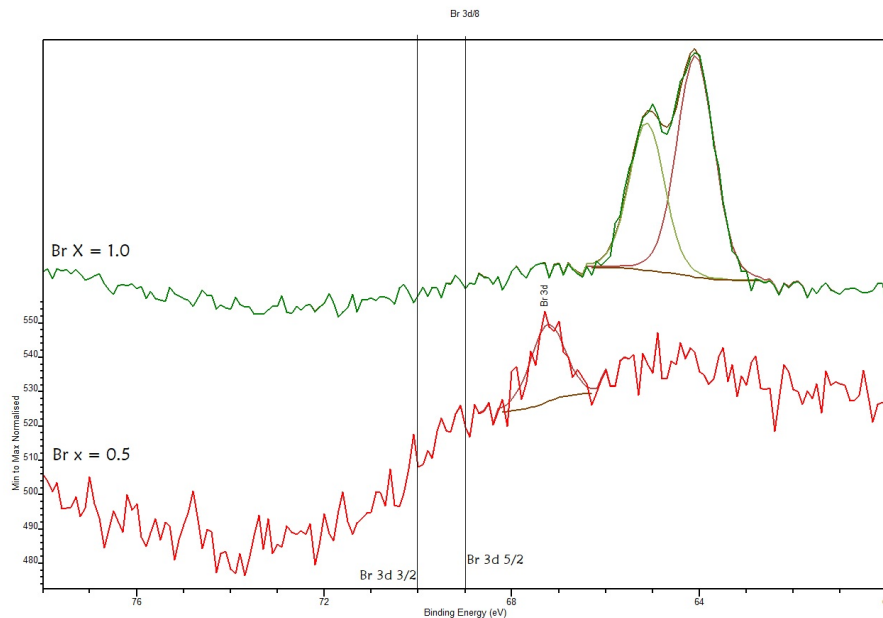
Figure 35. XPS survey scan showing presence of Br 3d signal performed on 09/12/20, though the positions of the photoelectron peaks have shifted to higher binding energies by approximately 3 eV. This could inidicate the Br is bound as an alternate chemical species or a result of sample charging effects. [68].

The evidence that Br is detectable highlight an important distinction between Cl and Br substitution. Doping of Br at high concentrations are able to produce a stable phase where as, high concentrations of Cl are either preferentially located towards the substrate surface, exceeding the penetration depth of the instrument or volatile Cl compounds are evaporating before measurement.
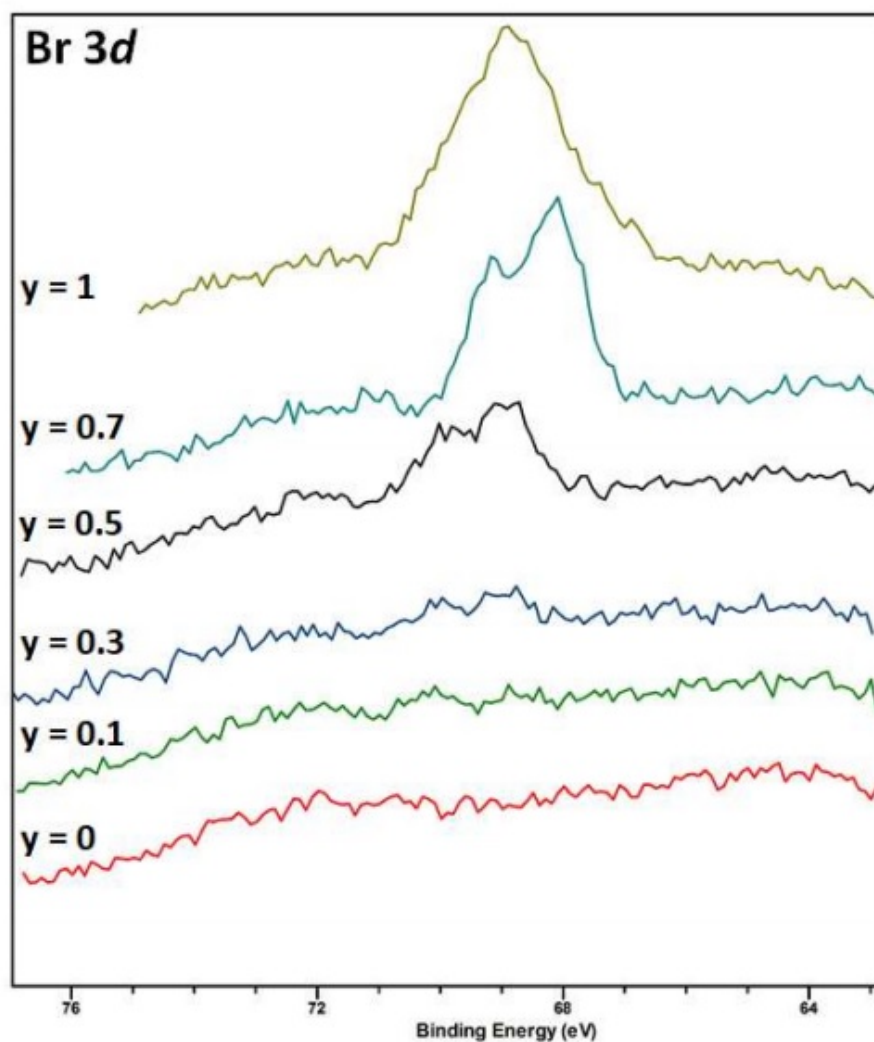
Figure 36. High resolution XPS spectra for Br 3d region
(25/06/18) [39]

 The figure above shows the Br $3d_{5/2}$ signal appearing at 68.9 eV compared to figure 35 where Br signal has shifted to approx 67.2 eV for X = 0.5 and a doublet feature occurring at approximately 64 eV for X = 1.0. The doublet feature has a separation energy of 1.05 eV which is characteristic of the Br ion. A difference of approximately 5 eV is apparent after 2 years of storage in a glove box suggesting the original $PbBr_2$ species is in an alternate oxidation state.

8.7 PL degradation

Due to the pandemic related interruption of study and potential decay of previous samples a new Cl doped perovskite series was synthesised - (F_Cl). Photoluminescence measurements were performed on said series as well as the initial Cl series (A_Cl). The peak positions, band gap and FWHM were determined for all samples in the fresh chlorine (F_Cl), aged chlorine (A_Cl) and aged bromine (A_Br) series' and plotted to illustrate changes.
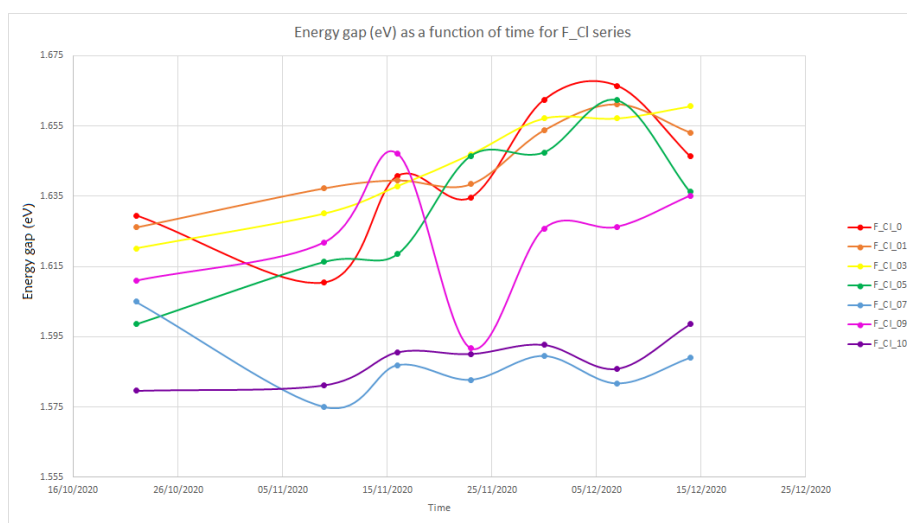

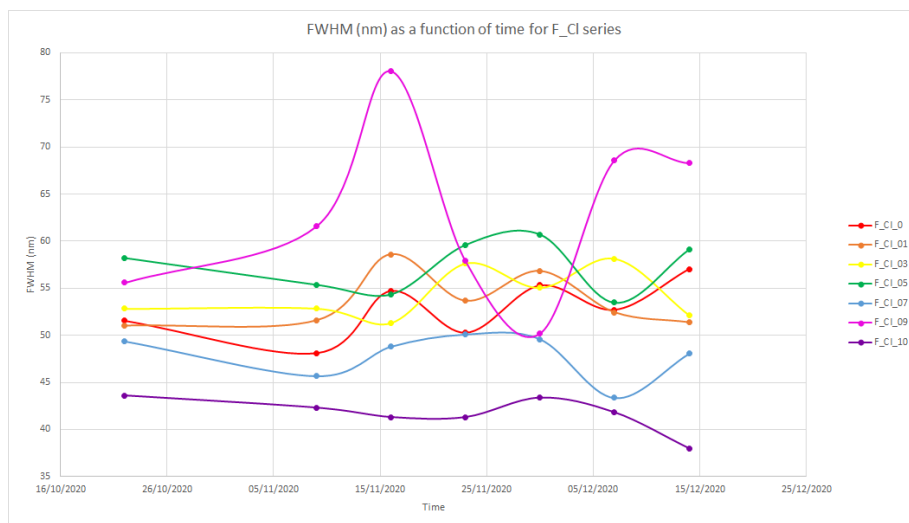Figure 37. Graph of energy gap as a function of time for fresh chlorine series F_Cl.

Figure 38. Graph of full width half max (FWHM) as a function of time for fresh chlorine series F_Cl.

From the figures above no pattern is obvious at first instance. However, between the first and second measurement, some degradation/chemical change has occurred due to the exposure to ambient air. Figure 38 shows all samples gradually increasing up until the third measurement. After this time, a pattern is difficult to discern as different regions of the sample have different stoichiometry. Most samples seem to plateau as band gap measurement approaches approximately 1.65 eV. This has been experimentally confirmed, within this study, to be the band gap of lead iodide. In particular 'F_Cl_09' (pink) behaves erratically in both figures 37 and 38. This is due to solubility issue of $PbCl_2$ in DMF and instability of perovskites with high Cl content.

Figure 38 shows the change in FWHM as a function of time, this data provides supporting evidence for degradation as changes in the FWHM are indicative of impurities that lead to broadening of the PL peak. The general trend of this series in this figure show an initial phase that partially decays into a mixture of the initial perovskite phase and degradation phase, until almost all of the intial perovskite has decayed into it's lead halide decay product. It is expected that FWHM will rise and then fall as remaining perovskite phase is converted into lead halide.

71

Again, it is worth mentioning 'F_Cl_09' (pink) behaves in much a similar way to figure 37, suggesting higher concentrations of Cl are detrimental to stability and the film consists of a mixture of target and non-target chemical species.

Further investigation into degradation and stability was undertaken by modelling peaks to data gathered by photoluminescence spectroscopy taken weekly across 7 weeks. As mentioned previously, PL measurements can be used to infer the purity of the sample and defects/impurities can lead to broadening of the PL peak.
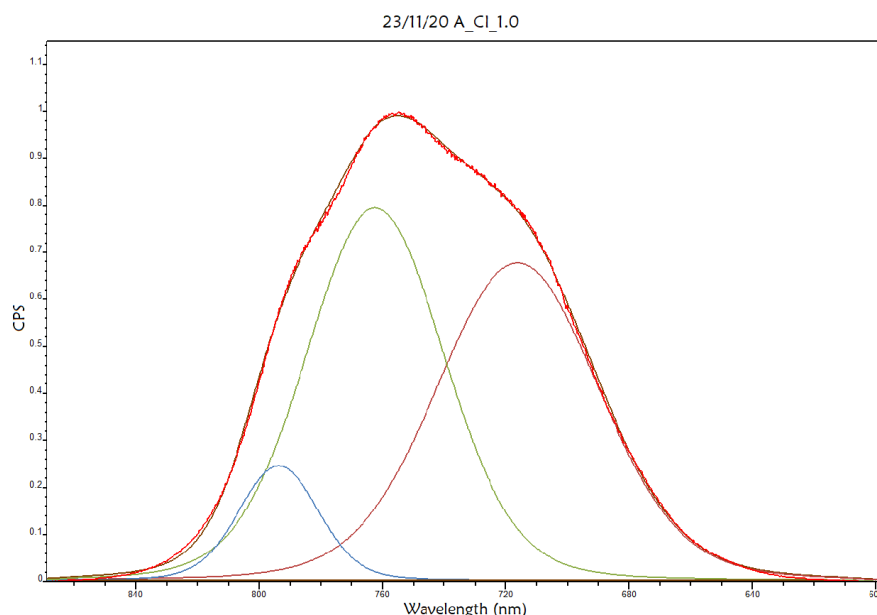

Figure 39. Above shows the main PL enveloping sub-peaks caused by impurity.

It is worth mentioning that literature reports changes to PL features due to excitation power of laser, exposure to environment and storage of perovskite prior to measurement [69]. The effect of nitrogen absorption on PL can result in the enhancement or attenuation of the Pl signal depending on the halide perovskite being measured and how long the sample was stored. Broadening can occur due to oxygen absorption and exposure to humidity in the environment. Other resources [70] provide an explanation of red/blue shifting of

PL spectra due to absorption of ambient moisture/gasses. Though, long term studies on the degradation of perovskite via PL measurements are difficult to find. As a comparison, two other series' A_Cl and A_Br (aged chlorine and aged bromine series, respectively).

Energy gap (eV) as a function of time for the A_Cl series

FWHM (nm) as a function of time for the A_Cl series

Figures 40 and 41 above illustrate the change in FWHM and E_g for the aged chlorine treated series (A_Cl). Figures display similar behaviour to F_Cl series.

The data in figure 40 shows a dramatic change after the first measurement due to being exposed to ambient air and by the second measurement, all samples seem to have a very similar energy gap. However, the FWHM corresponding to each concentration varies significantly. As mentioned before, high Cl concentrations introduce instability in the perovskite and its is understood that non-target phases are present within the sample such as: PbX_2, PbX_4 (X = I, Cl, Br). This can be clearly seen in figure 41 whereby the highest concentration (pink) exhibits a FWHM of approximately 110 nm as opposed to lower concentrations (orange) which possesses a FWHM of around 45 nm.

It is also worth mentioning here that lead chloride is not soluble in DMF and could be the main factor explaining the lack of Cl presence during XPS measurements. Despite this, Changes in PL peak position confirm influence of Cl in the perovskite. Initial PL data provided by H. Yates allows the comparison of 'fresh' Br doped perovskite with the parent sample, stored in a glove box. See figure below:
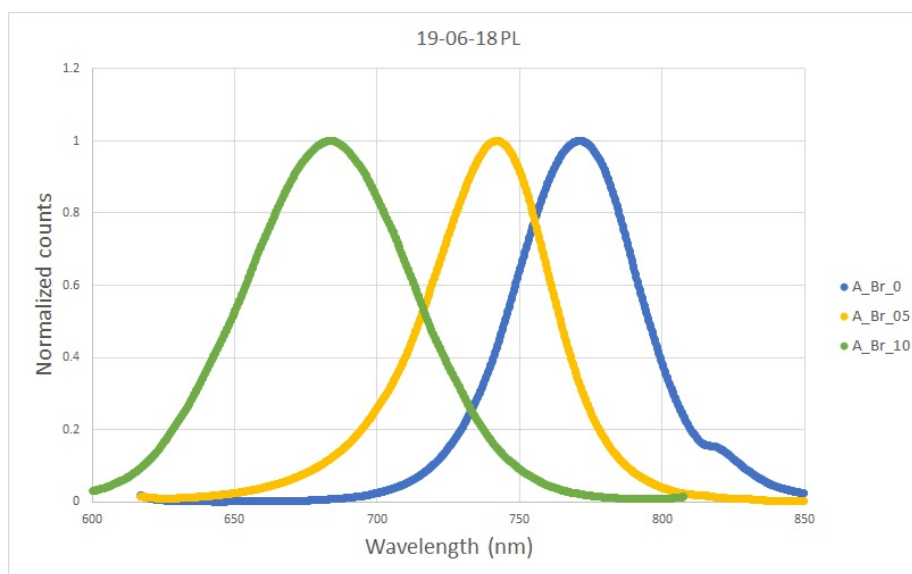

Figure 42. Initial PL measurements of Br doped perovskite performed on 19/06/18.

For ease, a table below summarises this series' peak position, energy gap and FWHM:

Table 23. Summary of information extracted from initial PL data.

Concentration	Peak position (nm)	Energy gap (eV)	FWHM (nm)
0	771.01	1.61	50.52
0.5	742.11	1.67	49.64
1.0	683.59	1.81	69.51

The table above shows that sample X = 1.0 possess the largest FWHM compared to lower concentrations. This suggests Br doping exhibits similar behaviour to Cl doping in the sense that higher concentrations tend to consist of more than just the target chemical species, as PL contributions from non-target/contaminant species are contained within the main PL peak - leading to broadening.
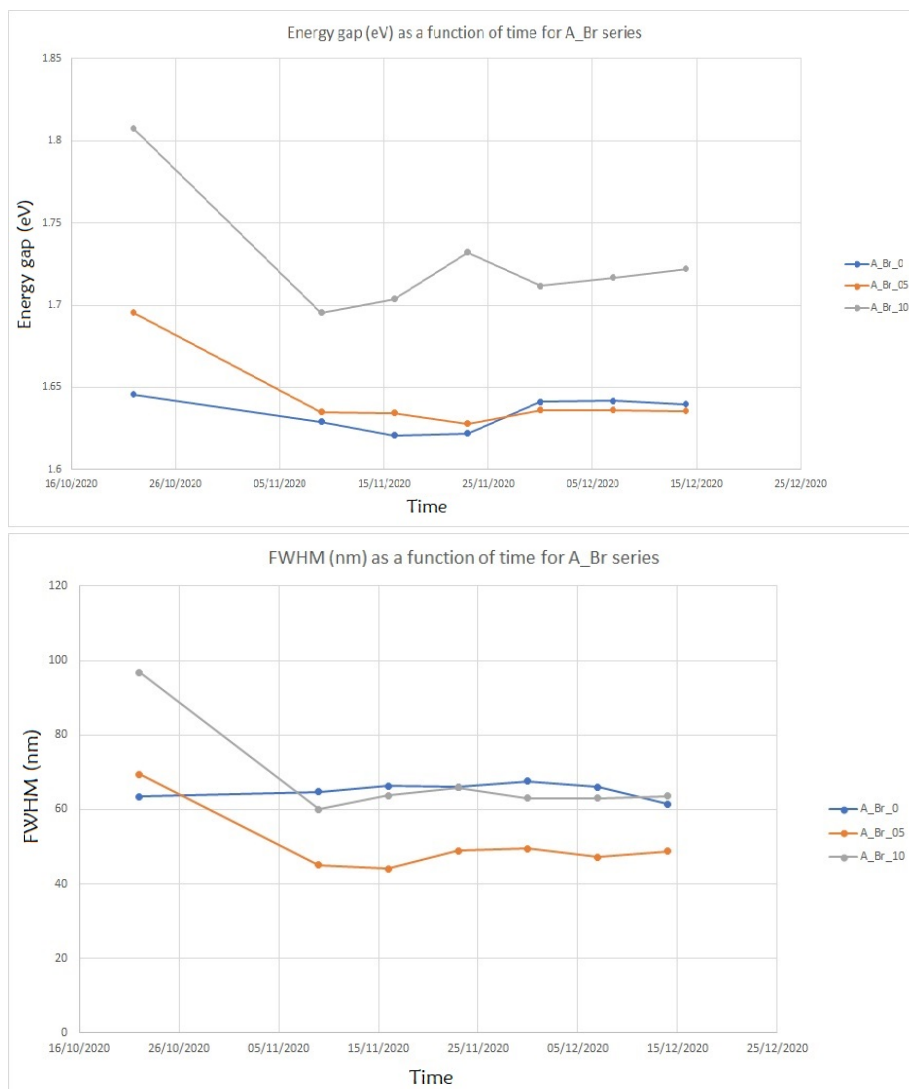
Figures 43 and 44. Show similar data for the three samples of Br treated (X = 0, 0.5 and 1.0).

By comparing the information gathered from figures 42, 43 and 44 it is evident that the initial energy gap measurement for X = 1.0 Br sample, is very close to the value determined 2 years later, suggesting that storage of samples in a glove box delayed degradation significantly. The values remain roughly the same despite age, though, dramatic changes in E_g and FWHM is observable in all samples after

76

initial exposure to ambient air. However, FWHM is much broader than initial 'fresh' samples with X = 1.0 showing a FWHM of close to 100 nm as opposed to $\approx 70nm$. This suggests that while a majority of the films composition remains unchanged, some non-target chemical species have formed during the time stored in the glove box.

Further measurements show not much change after exposure and E_g and FWHM remain within 5 nm of previous measurement. Similarly with Cl treated perovskite, Br rich samples have a significantly higher FWHM than lower concentrations. The Br samples are significantly older than A_Cl series (approx 2 years), yet display greater stability and a more consistent FWHM. The more stable FWHM in figure 50 suggests that the Br treated perovskite film is a lot more homogeneous and pristine than the highest Cl sample as the erratic behaviour from the CL series suggests that multiple phases are present in various regions of the sample.

8.7.1   Stability

The peak fitting revealed evidence to suggest perovskite treated with high concentrations of Cl were less stable than that of Br treated perovskites.
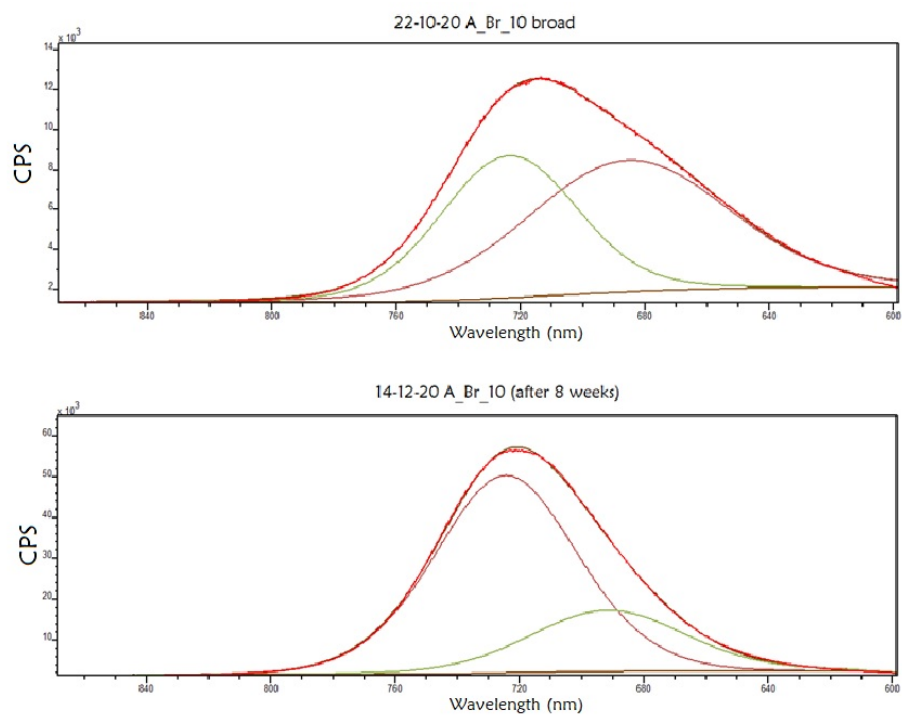
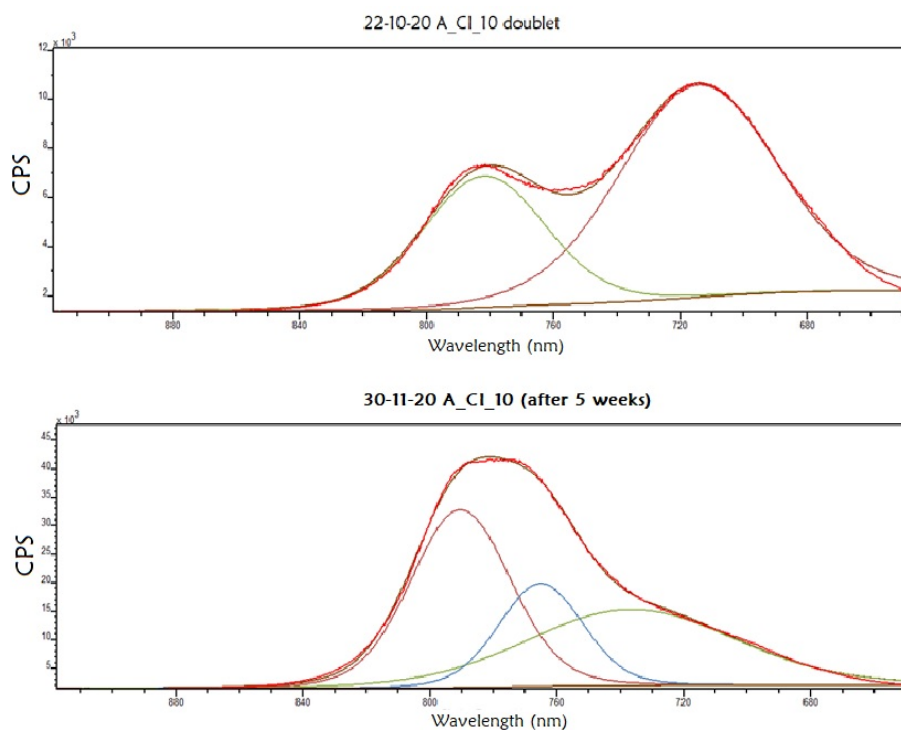Figure 45. Shows the evolution of PL peak for aged Br series (X = 1.0) after 8 weeks.

Figure 46. Shows the evolution of PL peak for aged Cl series (X = 1.0) after just 5 weeks

A comparison of figure 45 and figure 46 shows the PL measurements of Br treated perovskite and Cl treated perovskite. The top images in each figure illustrate the PL peak taken on the same day and already, the Cl treated sample is exhibiting distinct doublet feature belonging to different chemical species, while the Br treated sample exhibits a broad PL peak that enveloped impurity peaks. After 8 weeks, the Br sample still maintains a single, broad PL emission with the existence of 2 distinct chemical phases. However, after just 5 weeks the Cl treated sample has developed a third impurity phase contained within the main peak and the relative amounts of each phase has changed significantly.

An attempt at determining the identity of these sub-peaks via optical measurements was undertaken. So, PL measurements of the main decay products ($PbCl_2$, PbI_2 and $PbBr_2$) were recorded.

PbX_2 powders were stuck to glass slides using a drop of IPA and PL measurements between the range of 600 - 850 nm were taken. This produced no PL feature within this range, suggesting the band gap of PbX_2 precursors (X = Cl, Br) lies outside of this range and or the impurity peaks belong to other reaction products such as PbX_4 and MAX. Online resources [71] provide estimated band gaps using DFT: $PbBr_2 = 3.053$ eV, $PbCl_2 = 3.833$ eV and $PbI_2 = 2.413$ eV. However, these values are subject to scrutiny as the estimations are often under/over-estimated by approximately 40% and have been known to disagree with experimental values by as much as 50%.
In this study, the band gap of PbI_2 was experimentally determined to be closer to 1.7 eV.

Interestingly, aside from exposure to atmosphere, beam damage due to the laser can accelerate the decay of perovskite via photo and thermal channels. Below is a picture of how the focused beam has affected a sample.
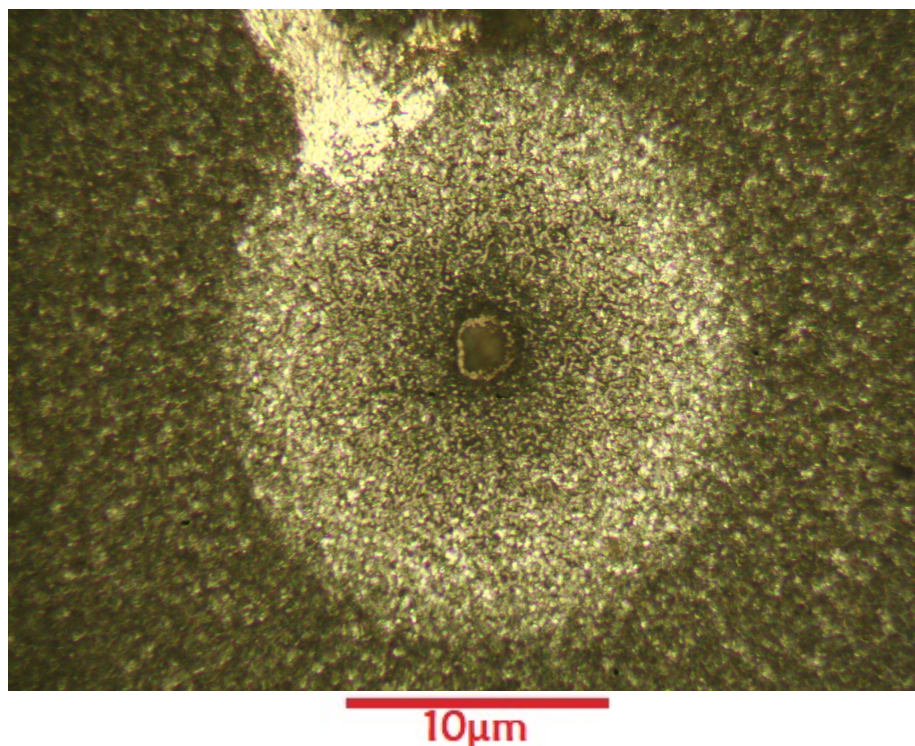

Figure 47. Image of beam damage on sample F_Cl_07

Structural Characterisation X-ray Diffraction was performed on a Bruker D8 Bragg-Brentano geometry and samples were run from 10° to 60° 2θ with a step size of 0.04° and step time of 0.5 seconds. Three samples of min, mid and max Cl concentration (X = 0, 0.5, 1.0) below, show diffractograms of each perovskite sample.
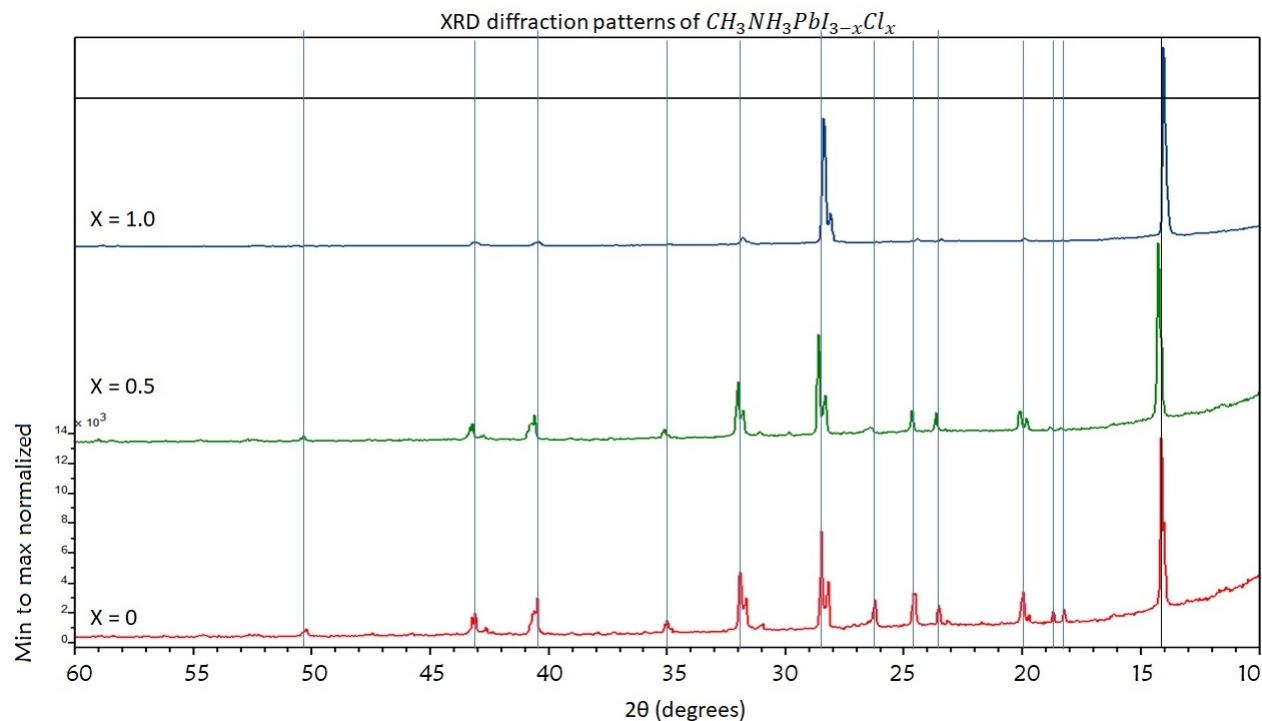

Figure 48. Overlaid diffractograms corresponding to each concentration.

XRD data shows predominantly tetragonal perovskite with a fraction of crystals possessing an orthorhombic structure indicating a polycrystalline film. The table below highlights the principal peak positions and the corresponding Miller indices.

Table 24. Summary of principal peak positions for each perovskite concentration and corresponding Miller indices hkl. Peak positions and Miller indices in the table above indicate tetragonal structure as the sum of hkl is equal to an even integer.

Sample	X = 0	hkl	X = 0.5	hkl	X = 1.0	hkl
	14.00	002	14.28	110	14.01	110
	14.16	110	19.85	112	19.80	112
	19.72	112	20.10	200	19.88	200
	19.96	200	23.66	2-11	23.36	2-11
	23.54	2-11	24.65	-202	24.35	202
	24.55	-202	28.32	004	28.05	004
	28.20	004	28.60	220	28.32	220
	28.47	220	31.79	-2-22	31.50	-2-20
	31.66	-2-22	32.01	130	31.77	130
	31.90	130	34.93	024	34.86	3-12
	34.81	024	35.09	3-12	40.34	224
	35.01	3-12	40.61	224	42.94	402
	40.49	224	43.19	402	50.10	-404
	43.10	402	43.32	3-30		
	43.22	3-30	50.33	-404		
	50.22	-404				

8.7.2 SEM & EDX

Each sample (X= 0, 0.5 and 1.0) was first coated with approximately 2 nm of Pt/Pd using the Cressington 208 sputter unite and were examined using FEI quant 250 ESEM. SEM micrographs were obtained using secondary electron detection system with magnifications of 1000x, 5000x and 10,000x respectively. EDX analysis involved spot probing particles as seen in the 10,000x mag images. Below show obtained SEM images and EDX spectra.
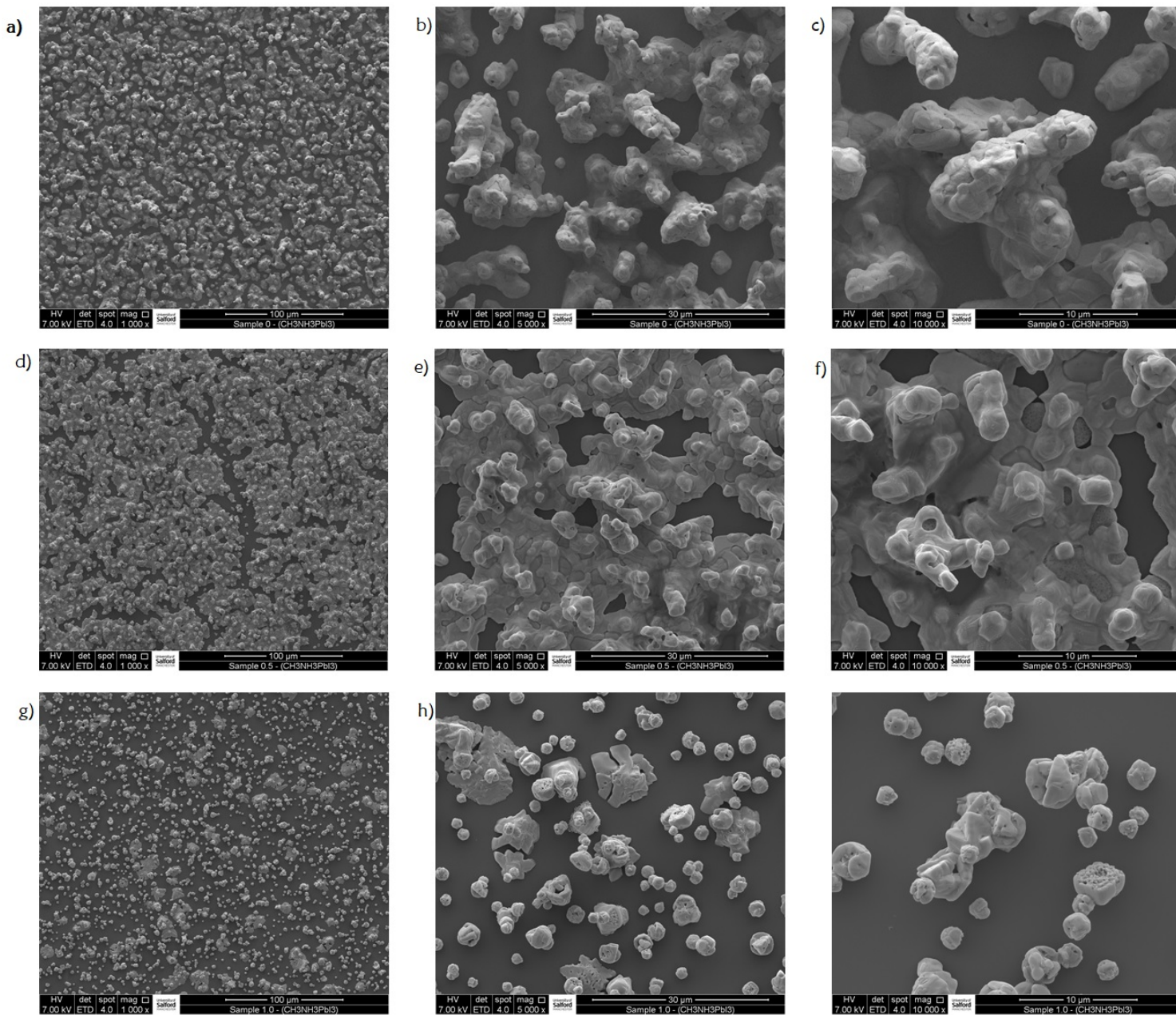
Figure 49. Images a), b) and c) correspond to untreated perovskite. d), e) and f) correspond to X = 0.5 and the last row of images correspond to X = 1.0 concentration.

Untreated sample images show distinct island formation that are mostly disconnected, this suggests that the particles are bound more tightly to each other than the substrate - hence island growth. Upon introduction of Cl (X = 0.5) morphology seems to improve with larger, more connected islands.

Unfortunately, maximum concentration of Cl (X = 1.0) shows very poor coverage, with isolated islands of growth. Post deposition of the X = 1.0 film, visual inspection suggested poor coverage as the film was very translucent. $PbCl_2$ is not very soluble in DMF and thus is suspected to be the main factor influencing this poor result. It has been suggested that improved morphology can be achieved by mixing DMF and DMSO in a 1:1 molar ratio [72]. In addition, the Relative Sensitivity Factors (RSF) used for the quantitative analysis of XPS spectra show that the RSF for bromine (0.853 - 1.279 eV for $3p_{3/2}$) [73] is an order of magnitude lower than the RSF for iodine (13.77 - 33.64 eV for $3d$) [73] and for chlorine is 0.775 - 2.285 eV [73]. Chlorine is apparently more sensitive to detection but evidence within this study and literature would disagree, this would imply that Cl resides beyond the penetration depth for the frequency of X-rays used.

EDX measurements confirmed the absence of Cl, this is thought to be primarily due to solubility issue during solution processing. Internal sources suggest that Cl peaks exist around 2.6 and 2.8 keV, though Pb and Pd have characteristic peaks at around 2.6 and 2.8 keV, respectively - 'washing out' the weak Cl signal [63].
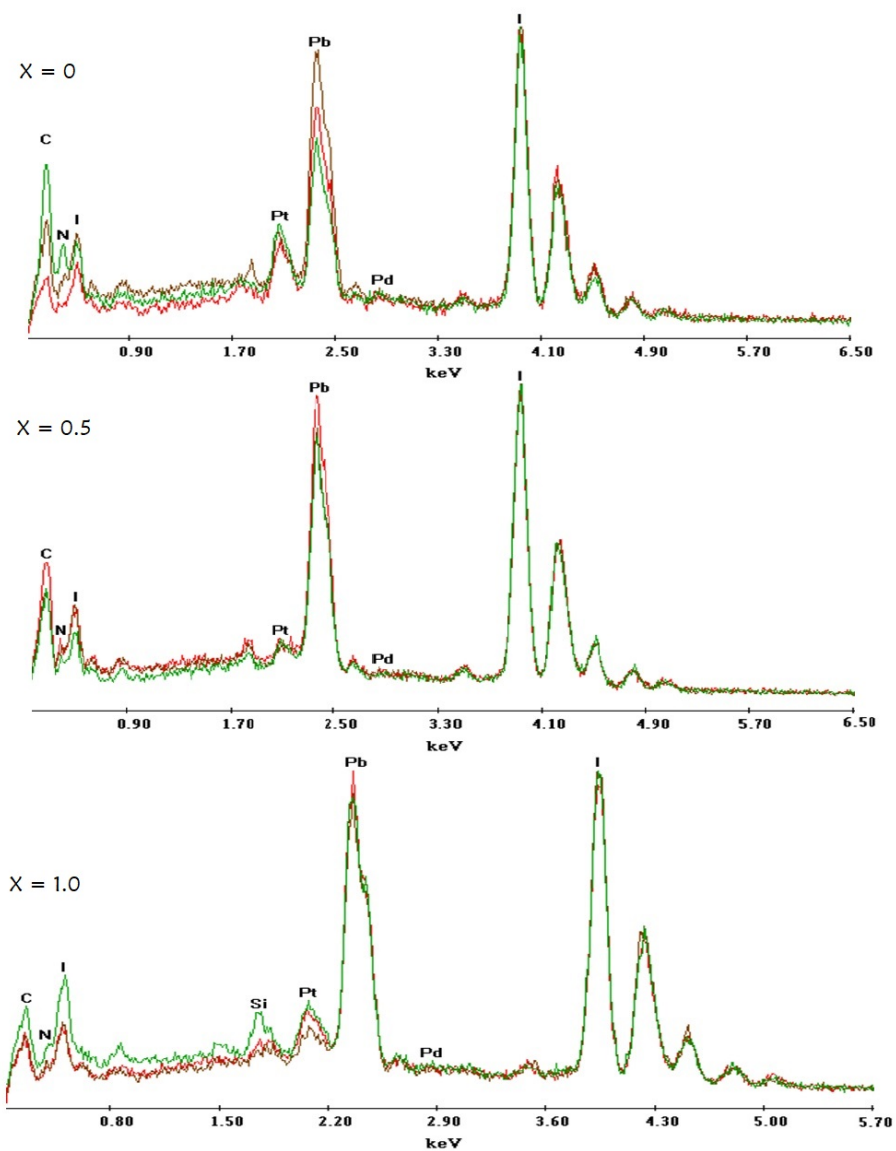
Figure 50. EDX spectra of Cl treated perovskite.

Aside from chemical presence, a small peak at approximately 1.8 keV corresponding to Si from the substrate, suggests that films were generally quite thin. Maximum Cl concentration reveals a significantly higher level of Si than lower concentrations, as expected with a very thin and meagre coverage of substrate. It is also observed that there is significantly less carbon present within the X

= 1.0 sample thus, it remains possible that volatile chlorocarbons form and evaporate during synthesis/deposition. Further internal research has confirmed a mixed solvent approach to the deposition of Cl treated perovskite results in better coverage and improved morphology, see below:
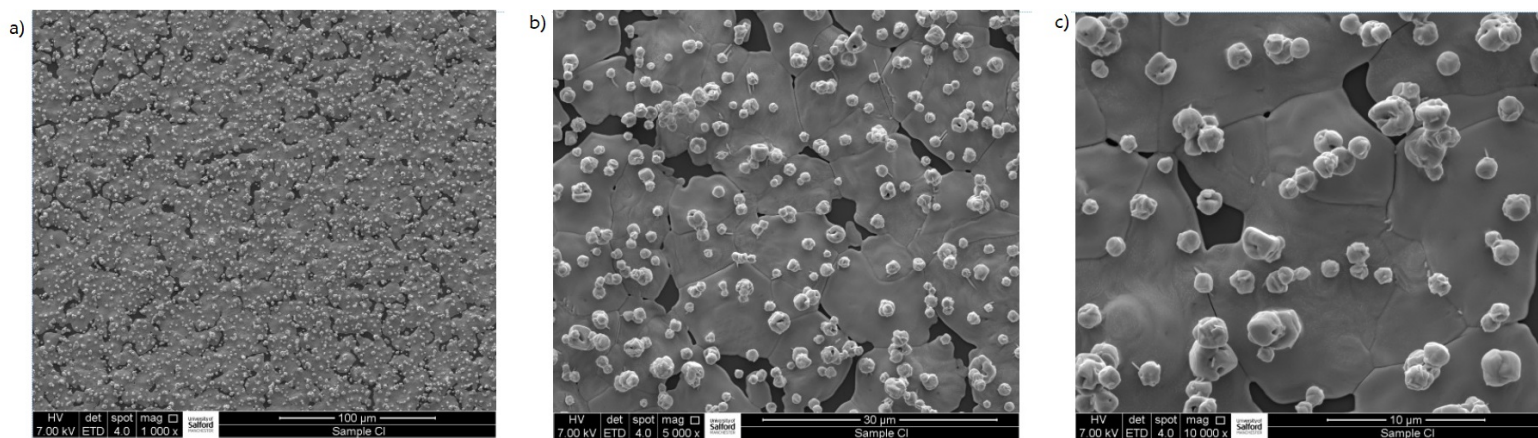
Figure 51. SEM images of Cl treated perovskite sample X = 1.0 synthesised using a 1:1 molar ratio of DMF:DMSO.

SEM images above show large, connected islands with clear morphological improvements compared with the corresponding images in figure 50. This provides strong evidence to support enhanced solubility of $PbCl_2$ in mixed solvent (DMF/DMSO) and enhanced morphology due to the presence of chlorine. In an attempt to confirm this, EDX spectra (below) were taken of the sample.
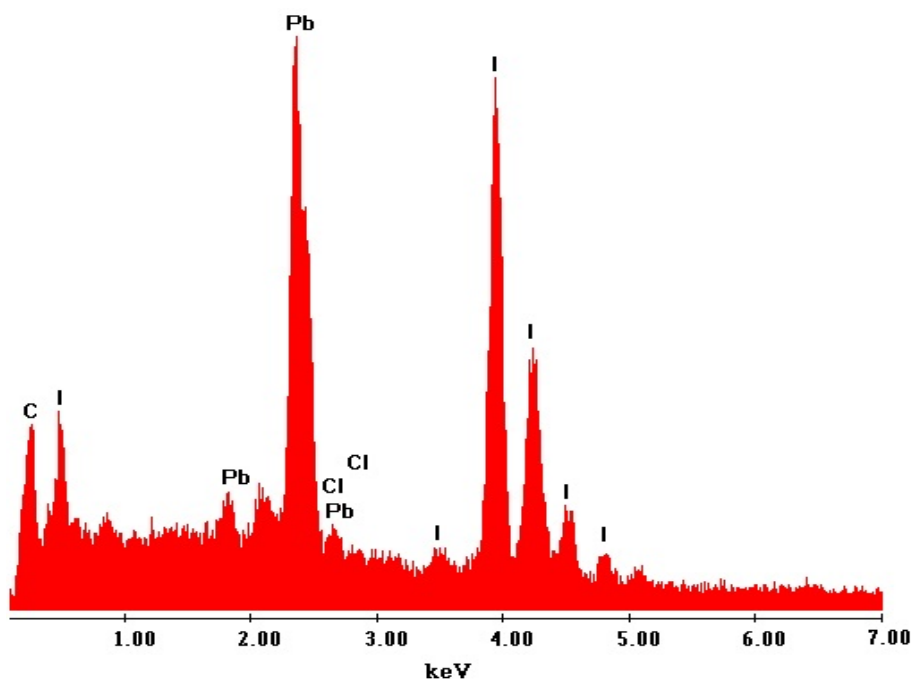
Figure 52. EDX spectra of Cl treated sample X = 1.0 synthesised using a 1:1 molar ratio of DMF:DMSO.

As mentioned earlier, Pb exhibits a peak in very close proximity to Cl making it difficult to resolve, this spectrum however confirms the presence of Cl at approximately 2.8 keV, further attributed to the mixed solvent synthesis. EDX being a bulk analytical technique provided a greater chance at detecting a chlorine signal than XPS due to the external X-ray source used during XPS and probing depth being the limiting factor. Where as, EDX detects the X-rays emitted from within the sample, providing a bulk analysis of elemental presence.
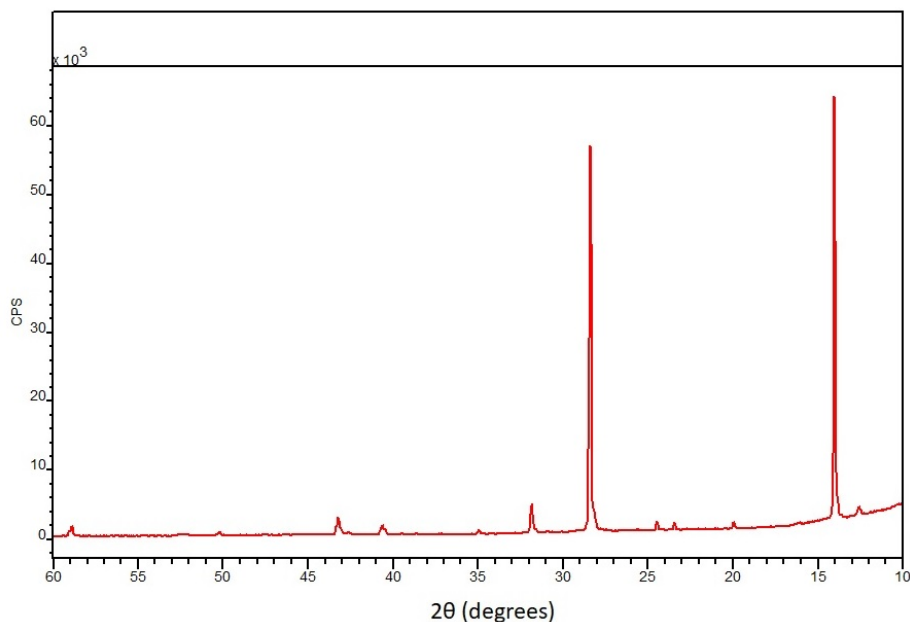
Figure 53. Illustrating diffractogram of mixed solvent Cl
perovskite.

XRD measuremnts of the mixed solvent Cl sample (above) show
very narrow peaks, indicative of improved crystallinity as opposed
to single solvent sample (figure 48). A summary of principal peak
positions also provided below:

Table 25. Summary of information extracted from initial PL data.

Concentration	Principal Peak position (2θ)	Miller index (hkl)
1.0	14.07	110
	20.01	200
	23.37	2-11
	24.48	202
	28.52	004
	31.82	-2-20
	35.01	3-12
	40.59	224
	43.21	402
	50.21	-404

From the summary above, a comparison between a mixed solvent synthesis and a single solvent synthesis can be made, differences in peak position of up to 0.11° 2θ. This is largely attributed to a higher amount of Cl successfully dissolving into the precursor solution and being incorporated into the final film as more Cl would contract lattice parameters, resulting in a shift towards higher angles. As previously, the structure is of tetragonal type, confirming the target species has been formed with improved morphology and crystallinity as a result of mixed solvent (DMF/DMSO) synthesis.

9 Chapter 5

10 Conclusion

In conclusion, mixed halide lead based perovskite thin films have been synthesised using AACVD and a detailed evaluation of the optical and morphological properties has been presented. This work demonstrates the process of AACVD can be improved by monitoring a few critical parameters such as: substrate position, temperature, nebulisation rate and duration.

Treating MAPI with Cl resulted in poorer quality films with a low degree of coverage, small and independent islands and not very opaque to the eye (indicative of film thickness), but this is attributed to the solvent used as $PbCl_2$ is not very soluble in DMF alone and requires a 1:1 mixture of DMF:DMSO. Optical measurements indicate that higher concentrations of $PbCl_2$ result in greater instability and the existence of multiple distinct phases as opposed to Br treated and MAPI. Although, when 'freshness' of the sample is considered, Cl treated perovskites exhibited a sharper, more dramatic absorption edge compared to lower concentrations so if the issue of stability could be managed, Cl treatment is viable for enhancing charge dynamics of perovskite. Lower Cl concentrations appear to improve morphology, resulting in larger islands with a greater degree of connectivity. Using mixed solvent (DMF:DMSO) during the synthesis of Cl treated perovskite resulted in clear morphological improvement and higher Cl levels residing in the film.

Optical measurements have confirmed optoelectronic influence due to Cl incorporation in the form of PL peak position changing by upto 50 nm, corresponding to a change in band gap of 0.25 eV. However, Cl has been absent from spectra where elemental identification is possible, but this is primarily due to the insolubility of $PbCl_2$ in DMF and the evaporation of volatile compounds during the deposition process. Br doped perovskite displayed improved stability and elemental Br was detected using XPS. Part of the results from this investigation were presented at the international conference of "SPIE Optics and Photonics", August 2020, San Diego, United States. Also part of these results will be also present in the coming international conference of "PVSAT-16", April 2022, Salford, United Kingdom.

11 Further research

This study has been negatively impacted due to COVID-19 pandemic and closure of required facilities. With this in mind, it is worth summarising that despite the lack of detection, Cl clearly influences the optoelectronic properties of these lead based perovskites. Further research to assess the role of Cl in these perovskites would be to modify the solvent from DMF to a 1:1 molar mixture of DMF:DMSO when synthesising as this improves the solubility of $PbCl_2$ and resulting in a higher quality film.

In order to develop this research further a complementary study combining the information generated by the analytical techniques used in this study with DFT calculations should be undertaken. A theoretical investigation into how Cl treatment affects band structure and density of states should be undertaken in support of this experimental data. The information generated by these methods will more precisely guide our understanding of the physics of these materials and eventually enable us to design PV enhancing devices with rationale.

References

[1] Brian O'Regan and Michael Gratzel. A low-cost, high-efficiency solar cell based on dye-sensitized colloidal tio2 films. *nature*, 353(6346):737, 1991.

[2] Akihiro Kojima, Kenjiro Teshima, Yasuo Shirai, and Tsutomu Miyasaka. Organometal halide perovskites as visible-light sensitizers for photovoltaic cells. *Journal of the American Chemical Society*, 131(17):6050–6051, 2009.

[3] Zhengguo Xiao, Qingfeng Dong, Cheng Bi, Yuchuan Shao, Yongbo Yuan, and Jinsong Huang. Solvent annealing of perovskite-induced crystal growth for photovoltaic-device efficiency enhancement. *Advanced Materials*, 26(37):6503–6509, 2014.

[4] Devendra Khatiwada, Swaminathan Venkatesan, Nirmal Adhikari, Ashish Dubey, Abu Farzan Mitul, Lal Mohammad, Anastasiia Iefanova, Seth B Darling, and Qiquan Qiao. Efficient perovskite solar cells by temperature control in single and mixed halide precursor solutions and films. *The Journal of Physical Chemistry C*, 119(46):25747–25753, 2015.

[5] Marina Leontiadou. *Nanostructured Materials for Type III Photovoltaics, chapter 14*. Royal Society of Chemistry, 2017.

[6] Zhi-Kuang Tan, Reza Saberi Moghaddam, May Ling Lai, Pablo Docampo, Ruben Higler, Felix Deschler, Michael Price, Aditya Sadhanala, Luis M Pazos, Dan Credgington, et al. Bright light-emitting diodes based on organometal halide perovskite. *Nature nanotechnology*, 9(9):687–692, 2014.

[7] Felix Deschler, Michael Price, Sandeep Pathak, Lina E Klintberg, David-Dominik Jarausch, Ruben Higler, Sven Hüttner, Tomas Leijtens, Samuel D Stranks, Henry J Snaith, et al. High photoluminescence efficiency and optically pumped lasing in solution-processed mixed halide perovskite semiconductors. *J. Phys. Chem. Lett*, 5(8):1421–1426, 2014.

[8] Sarah Brittman, Gede Widia Pratama Adhyaksa, and Erik Christian Garnett. The expanding world of hybrid per-

ovskites: materials properties and emerging applications. *MRS communications*, 5(1):7–26, 2015.

[9] Marc De Graef and Michael E McHenry. *Structure of materials: an introduction to crystallography, diffraction and symmetry.* Cambridge University Press, 2012.

[10] V. M. Goldschmidt. Crystal structure and chemical constitution. *Trans. Faraday Soc.*, 25:253–283, 1929.

[11] Chonghea Li, Xionggang Lu, Weizhong Ding, Liming Feng, Yonghui Gao, and Ziming Guo. Formability of abx3 (x= f, cl, br, i) halide perovskites. *Acta Crystallographica Section B: Structural Science*, 64(6):702–707, 2008.

[12] Jun Hong Noh, Sang Hyuk Im, Jin Hyuck Heo, Tarak N. Mandal, and Sang Il Seok. Chemical management for colorful, efficient, and stable inorganic–organic hybrid nanostructured solar cells. *Nano Letters*, 13(4):1764–1769, 2013.

[13] Xing Zhao and Nam-Gyu Park. Stability issues on perovskite solar cells. *Photonics*, 2:1139–1151, 11 2015.

[14] 'Carsten Schinzer'. tolerance factor and perovskite structure distortion of perovskites. Accessed: 20/12/19.

[15] Chonghea Li, Xionggang Lu, Weizhong Ding, Liming Feng, Yonghui Gao, and Ziming Guo. Formability of abx3 (x= f, cl, br, i) halide perovskites. *Acta Crystallographica Section B: Structural Science*, 64(6):702–707, 2008.

[16] Jun Hong Noh, Sang Hyuk Im, Jin Hyuck Heo, Tarak N Mandal, and Sang Il Seok. Chemical management for colorful, efficient, and stable inorganic–organic hybrid nanostructured solar cells. *Nano letters*, 13(4):1764–1769, 2013.

[17] Javeed Akhtar, Muhammad Aamir, and Muhammad Sher. Chapter 2 - organometal lead halide perovskite. *Academic Press*, Perovskite Photovoltaics:25 – 42, 2018.

[18] SY Yang, Jan Seidel, SJ Byrnes, P Shafer, C-H Yang, MD Rossell, P Yu, Y-H Chu, JF Scott, JW Ager Iii, et al. Above-bandgap voltages from ferroelectric photovoltaic devices. *Nature nanotechnology*, 5(2):143, 2010.

[19] Ilya Grinberg, D Vincent West, Maria Torres, Gaoyang Gou, David M Stein, Liyan Wu, Guannan Chen, Eric M Gallo, Andrew R Akbashev, Peter K Davies, et al. Perovskite oxides for visible-light-absorbing ferroelectric and photovoltaic materials. *Nature*, 503(7477):509, 2013.

[20] Dominic W. Ferdani, Samuel R. Pering, Dibyajyoti Ghosh, Peter Kubiak, Alison B. Walker, Simon E. Lewis, Andrew L. Johnson, Peter J. Baker, M. Saiful Islam, and Petra J. Cameron. artial cation substitution reduces iodide ion transport in lead iodide perovskite solar cells. *Energy Environ. Sci.*, 12:2264–2272, 2019.

[21] Tze-Bin Song, Qi Chen, Huanping Zhou, Chengyang Jiang, Hsin-Hua Wang, Yang Michael Yang, Yongsheng Liu, Jingbi You, and Yang Yang. Perovskite solar cells: film formation and properties. *Journal of Materials Chemistry A*, 3(17):9032–9050, 2015.

[22] Dhana Lakshmi Busipalli, Santhanamoorthi Nachimuthu, and Jyh-Chiang Jiang. Theoretical study on halide and mixed halide perovskite solar cells: Effects of halide atoms on the stability and electronic properties. *Journal of the Chinese Chemical Society*, 66(6):575–582, 2019.

[23] Mark T Anderson, Kevin B Greenwood, Gregg A Taylor, and Kenneth R Poeppelmeier. B-cation arrangements in double perovskites. *Progress in solid state chemistry*, 22(3):197–233, 1993.

[24] Kui Qin, Binghai Dong, and Shimin Wang. Improving the stability of metal halide perovskite solar cells from material to structure. *Journal of energy chemistry*, 33:90–99, 2019.

[25] Simone Meloni, Giulia Palermo, Negar Ashari Astani, Basile FE Curchod, Michael Graetzel, and Ursula Roethlisberger. Valence and conduction bands engineering in halide perovskites for solar cell applica-tions. *arXiv preprint arXiv:1412.3659*, 2014.

[26] Liujiang Zhou, Claudine Katan, Wanyi Nie, Hsinhan Tsai, Laurent Pedesseau, Jared J Crochet, Jacky Even, Aditya D Mohite, Sergei Tretiak, and Amanda J Neukirch. Cation alloying delocalizes polarons in lead halide perovskites. *The journal of physical chemistry letters*, 10(13):3516–3524, 2019.

[27] H Mashiyama, Y Kurihara, and T Azetsu. Disordered cubic perovskite structure of ch˜ 3 nh˜ 3pbx˜ 3 (x= ci, br, i). *JOURNAL-KOREAN PHYSICAL SOCIETY*, 32:S156–S158, 1998.

[28] Fengyu Li, Fuzhao Yi, Junfeng Gao, Haijun Zhang, and Zhongfang Chen. Modulating the electronic properties of perovskite via σ–π interfacial interactions: A computational study. *APL Materials*, 6(11):114203, 2018.

[29] Fang Yuan, Chenxin Ran, Lin Zhang, Hua Dong, Bo Jiao, Xun Hou, Jingrui Li, and Zhaoxin Wu. A cocktail of multiple cations in inorganic halide perovskite toward efficient and highly stable blue light-emitting diodes. *ACS Energy Letters*, 5(4):1062–1069, 2020.

[30] Jeremy Barnett, Vivien Cherrette, Connor Hutcherson, and Monica So. Effects of solution-based fabrication conditions on morphology of lead halide perovskite thin film solar cells. *Advances in Materials Science and Engineering*, 2016:1–12, 01 2016.

[31] Yicheng Zhao, Jing Wei, Heng Li, Yin Yan, Wenke Zhou, Dapeng Yu, and Qing Zhao. A polymer scaffold for self-healing perovskite solar cells. *Nature Communications*, page 10:228, 2016.

[32] Nurul Ain Manshor, Qamar Wali, Ka Kan Wong, Saifful Kamaluddin Muzakir, Azhar Fakharuddin, Lukas Schmidt-Mende, and Rajan Jose. Humidity versus photo-stability of metal halide perovskite films in a polymer matrix. *Physical Chemistry Chemical Physics*, 18(31):21629–21639, 2016.

[33] Tanzila Tasnim Ava, Abdullah Al Mamun, Sylvain Marsillac, and Gon Namkoong. A review: thermal stability of methylammonium lead halide based perovskite solar cells. *Applied Sciences*, 9(1):188, 2019.

[34] Sam Zhang and Guifang Han. Intrinsic and environmental stability issues of perovskite photovoltaics. *Progress in Energy*, 2(2):022002, 2020.

[35] Qi Chen, Huanping Zhou, Yihao Fang, Adam Z Stieg, Tze-Bin Song, Hsin-Hua Wang, Xiaobao Xu, Yongsheng Liu, Shirong Lu, Jingbi You, et al. The optoelectronic role of chlorine in ch 3 nh 3 pbi 3 (cl)-based perovskite solar cells. *Nature communications*, 6:7269, 2015.

[36] Spencer T Williams, Fan Zuo, Chu-Chen Chueh, Chien-Yi Liao, Po-Wei Liang, and Alex K-Y Jen. Role of chloride in the morphological evolution of organo-lead halide perovskite thin films. *ACS nano*, 8(10):10640–10654, 2014.

[37] Lin Fan, Yi Ding, Jingshan Luo, Biao Shi, Xin Yao, Changchun Wei, Dekun Zhang, Guangcai Wang, Yun Sheng, Yifeng Chen, et al. Elucidating the role of chlorine in perovskite solar cells. *Journal of Materials Chemistry A*, 5(16):7423–7432, 2017.

[38] Silvia Colella, Edoardo Mosconi, Paolo Fedeli, Andrea Listorti, Francesco Gazza, Fabio Orlandi, Patrizia Ferro, Tullo Besagni, Aurora Rizzo, Gianluca Calestani, et al. Mapbi3-xcl x mixed halide perovskite for hybrid solar cells: the role of chloride as dopant on the transport and structural properties. *Chemistry of Materials*, 25(22):4613–4618, 2013.

[39] Shreya Basak, Mohammad Afzaal, and Heather M Yates. Optically tuned and large-grained bromine doped ch3nh3pbi3 perovskite thin films via aerosol-assisted chemical vapour deposition. *Materials chemistry and physics*, 223:157–163, 2019.

[40] Muhamad Z Mokhtar, Qian Chen, Qing Lian, David J Lewis, Brian R Saunders, Alex S Walton, Chun-Ren Ke, Eric Whittaker, Bruce Hamilton, and Saif Haque. Decoupling structure and composition of ch3nh3pbi3–x br x films prepared by combined one-step and two-step deposition. *ACS Applied Energy Materials*, 1(10):5567–5578, 2018.

[41] Mu Chen, Muhamad Z Mokhtar, Eric Whittaker, Qing Lian, Bruce Hamilton, Paul O'Brien, Mingning Zhu, Zhengxing Cui, Saif A Haque, and Brian R Saunders. Reducing hole transporter use and increasing perovskite solar cell stability with dual-role polystyrene microgel particles. *Nanoscale*, 9(28):10126–10137, 2017.

[42] Yichuan Chen, Linrui Zhang, Yongzhe Zhang, Hongli Gao, and Hui Yan. Large-area perovskite solar cells–a review of recent progress and issues. *RSC advances*, 8(19):10489–10508, 2018.

[43] Francesca De Rossi, Jenny A Baker, David Beynon, Katherine EA Hooper, Simone MP Meroni, Daniel Williams, Zhengfei Wei, Amrita Yasin, Cecile Charbonneau, Eifion H Jewell, et al. All printable perovskite solar modules with 198 cm^2 active area and over 6% efficiency. *Advanced Materials Technologies*, 3(11):1800156, 2018.

[44] DS Bhachu, DO Scanlon, EJ Saban, H Bronstein, IP Parkin, CJ Carmalt, and RG Palgrave. Scalable route to ch 3 nh 3 pbi 3 perovskite thin films by aerosol assisted chemical vapour deposition. *Journal of Materials Chemistry A*, 3(17):9071–9073, 2015.

[45] Mohammad Afzaal and Heather M Yates. Growth patterns and properties of aerosol-assisted chemical vapor deposition of $ch_3nh_3pbi_3$ films in a single step. *Surface and Coatings Technology*, 321:336–340, 2017.

[46] Esteban Climent-Pascual, Bruno Clasen Hames, Jorge S Moreno-Ramírez, Angel Luis Álvarez, Emilio J Juarez-Perez, Elena Mas-Marza, Ivan Mora-Seró, Alicia De Andrés, and Carmen Coya. Influence of the substrate on the bulk properties of hybrid lead halide perovskite films. *Journal of Materials Chemistry A*, 4(46):18153–18163, 2016.

[47] Selina Olthof and Klaus Meerholz. Substrate-dependent electronic structure and film formation of mapbi 3 perovskites. *Scientific reports*, 7(1):1–10, 2017.

[48] Heather Yates. Thin films and materials characterisation. *unpublished*, accessed 2020.

[49] Yonghua Chen, Tao Chen, and Liming Dai. Layer-by-layer growth of ch3nh3pbi3- xclx for highly efficient planar heterojunction perovskite solar cells. *Advanced Materials*, 27(6):1053–1059, 2015.

[50] Feng Zhang, Haizheng Zhong, Cheng Chen, Xian-gang Wu, Xiangmin Hu, Hailong Huang, Junbo Han, Bingsuo Zou, and

Yuping Dong. Brightly luminescent and color-tunable colloidal ch3nh3pbx3 (x= br, i, cl) quantum dots: potential alternatives for display technology. *ACS nano*, 9(4):4533–4542, 2015.

[51] IB Koutselas, Laurent Ducasse, and George C Papavassiliou. Electronic properties of three-and low-dimensional semiconducting materials with pb halide and sn halide units. *Journal of Physics: Condensed Matter*, 8(9):1217, 1996.

[52] Chaminda Lakmal Hettiarachchi. Organometal halide perovskite solar absorbers and ferroelectric nanocomposites for harvesting solar energy. 2017.

[53] Alexander R Pascoe, Mengjin Yang, Nikos Kopidakis, Kai Zhu, Matthew O Reese, Garry Rumbles, Monika Fekete, Noel W Duffy, and Yi-Bing Cheng. Planar versus mesoscopic perovskite microstructures: The influence of ch3nh3pbi3 morphology on charge transport and recombination dynamics. *Nano Energy*, 22:439–452, 2016.

[54] Yantao Shi, Yujin Xing, Yu Li, Qingshun Dong, Kai Wang, Yi Du, Xiaogong Bai, Shufeng Wang, Zhijian Chen, and Tingli Ma. Ch3nh3pbi3 and ch3nh3pbi3–x cl x in planar or mesoporous perovskite solar cells: Comprehensive insight into the dependence of performance on architecture. *The Journal of Physical Chemistry C*, 119(28):15868–15873, 2015.

[55] Daniel Espinobarro-Velazquez, Marina A Leontiadou, Robert C Page, Marco Califano, Paul O'Brien, and David J Binks. Effect of chloride passivation on recombination dynamics in cdte colloidal quantum dots. *ChemPhysChem*, 16(6):1239–1244, 2015.

[56] Heinrich Hertz. Ueber einen einfluss des ultravioletten lichtes auf die electrische entladung. *Annalen der Physik*, 267(8):983–1000, 1887.

[57] Albert Einstein. Concerning an heuristic point of view toward the emission and transformation of light. *American Journal of Physics*, 33(5):367, 1965.

[58] Malgorzata Sowinska. In-operando hard x-ray photoelectron spectroscopy study on the resistive switching physics of hfo2-based rram. 2014.

[59] ' Batista'. Spin-orbit interaction. Accessed: 03/04/2020.

[60] 'Dr. Mark Biesinger'. Xps spin-orbit splitting. Accessed: 06/04/2020.

[61] accessed 02/21 Bruker D2 phaser internet brochure.

[62] accessed 03/21 Jeremy Carl Cockcroft.

[63] Geoff Parr. Private communications. Salford Analytical Services (SAS), 2021.

[64] Yolla Sukma Handayani, Efi Dwi Indari, Rahmat Hidayat, Yoshiyuki Othsubo, and Shin-ichi Kimura. Understanding the role of organic cations on the electronic structure of lead iodide perovskite from their uv photoemission spectra and their electronic structures calculated by dft method. *Materials Research Express*, 6(8):084009, 2019.

[65] Shreya Basak, Mohammad Afzaal, and Heather M Yates. Optically tuned and large-grained bromine doped ch3nh3pbi3 perovskite thin films via aerosol-assisted chemical vapour deposition. *Materials Chemistry and Physics*, 223:157–163, 2019.

[66] Haipeng Xie, Xiaoliang Liu, Lu Lyu, Dongmei Niu, Qi Wang, Jinsong Huang, and Yongli Gao. Effects of precursor ratios and annealing on electronic structure and surface composition of ch3nh3pbi3 perovskite films. *The Journal of Physical Chemistry C*, 120(1):215–220, 2016.

[67] Qi Chen, Huanping Zhou, Ziruo Hong, Song Luo, Hsin-Sheng Duan, Hsin-Hua Wang, Yongsheng Liu, Gang Li, and Yang Yang. Planar heterojunction perovskite solar cells via vapor-assisted solution process. *Journal of the American Chemical Society*, 136(2):622–625, 2014.

[68] H. Yates C. Gregory. Private communications. 2020.

[69] Jinlei Zhang, Jiuyang He, Lun Yang, and Zhixing Gan. Photoluminescent spectral broadening of lead halide perovskite nanocrystals investigated by emission wavelength dependent lifetime. *Molecules*, 25(5):1151, 2020.

[70] Sven Gerritson. Studying degradation of perovskite solar cells in ambient atmosphere using photoluminescence spectroscopy. *unpublished*, 2019.

[71] G. Hautier W. Chen W.D. Richards S. Dacek S. Cholia D. Gunter D. Skinner G. Ceder K.A. Persson (*=equal contributions) A. Jain*, S.P. Ong*. The materials project: A materials genome approach to accelerating materials innovation. 1.

[72] GW Warren and H Henein. Solubility of pbcl2 in dmso and dmso—water solutions. *Hydrometallurgy*, 46(1-2):243–247, 1997.

[73] M.C. Biesinger 2009-2020, 2009-2020.